

Low mass star formation and subclustering in the H II regions RCW 32, 33 and 27 of the Vela Molecular Ridge

A photometric diagnostics to identify M-type stars

L. Prisinzano¹, F. Damiani¹, M. G. Guarcello¹, G. Micela¹, S. Sciortino¹, E. Tognelli², and L. Venuti¹

¹ INAF - Osservatorio Astronomico di Palermo, Piazza del Parlamento 1, 90134, Palermo, Italy
e-mail: loredana.prisinzano@inaf.it

² Department of Physics 'E. Fermi', University of Pisa, Largo Bruno Pontecorvo 3, I-56127 Pisa, Italy

ABSTRACT

Context. Most stars born in clusters and recent results suggest that star formation (SF) preferentially occurs in subclusters. Studying the morphology and SF history of young clusters is crucial to understanding early cluster formation processes.

Aims. We aim to identify the embedded population of young stellar objects (YSOs) down to the low mass stars in the M-type regime, in the three H II regions RCW 33, RCW 32 and RCW 27 located in the northwestern region of the Vela Molecular Ridge. Our aim is to characterise their properties, such as morphology and extent of the clusters in the three H II regions, derive stellar ages and the connection of the SF history with the environment.

Methods. Through public photometric surveys such as Gaia, VPHAS, 2MASS and Spitzer/GLIMPSE, we identify YSOs with classical techniques aimed at detecting IR, H α and UV excesses, as signature of circumstellar disks and accretion. In addition, we implement a method to distinguish main sequence (MS) stars and giants in the M-type regime, by comparing the reddening derived in several optical/IR color-color diagrams, assuming suitable theoretical models. Since this diagnostic is sensitive to stellar gravity, the procedure allows us to identify also pre-main sequence (PMS) stars.

Results. Using the classical membership criteria, we find a large population of YSOs showing signatures of circumstellar disks with or without accretion. In addition, with the new technique of M-type star selection, we find a rich population of young M-type stars with a spatial distribution strongly correlated to the more massive population. We find evidence of three young clusters, with different morphology, for which we estimate the individual distances by using TGAS Gaia data of the brighter subsample. In addition, we identify field stars falling in the same region, by securely classifying them as giants and foreground MS stars.

Conclusions. We identify the embedded population of YSOs, down to about 0.1 M $_{\odot}$, associated with the three H II regions RCW 33, RCW 32 and RCW 27 and the three clusters Vela T2, Cr 197 and Vela T1, respectively. All the three clusters are located at a similar distance but show very different morphologies. Our results suggest a decreasing SF rate in Vela T2 and triggered SF in Cr 197 and Vela T1.

Key words. techniques: photometric – stars: formation – pre-main sequence – stars: low mass, ISM: H II regions Galaxy: open clusters and associations: individual: RCW 33, RCW 32, RCW 27, Vela T1, Vela T2, Cr 291, stars: formation

1. Introduction

The Vela Molecular Ridge (VMR) is a large molecular cloud complex, revealed by four strong emission peaks observed in the 1 \rightarrow 0 transition of ¹²CO (Murphy & May, 1991), indicating that active SF is taking place (Pettersson, 2008). It is located in the constellations of Puppis and Vela and it is part of a complex region including the very large H II Gum Nebula, the Vela supernova remnant and also a remarkable annular system of cometary globules (Pettersson, 2008).

Murphy & May (1991) identified four main clouds within the VMR, named A, B, C and D, with the clouds A, C and D located at 0.7 \pm 0.2 kpc and the B cloud located a 2 kpc. Several small H II regions have also been found in this region. Liseau et al. (1992) and Lorenzetti et al. (1993) have found 33 class I objects in the VMR based on JHKL NIR photometry, of which 25 fall in clouds A, C and D and 8 in the cloud B. Other surveys based on NIR and CO observations have been conducted in the whole VMR region with the aim of finding signs of embedded YSOs. A detailed review is given in Pettersson (2008).

The northwestern region of the VMR, falling in cloud D has been the subject of an H α survey covering a 5 $^{\circ}$ 5' \times 5 $^{\circ}$ 5' field, centered on RA (1950)=8 $^{\text{h}}$ 43 $^{\text{m}}$ 2, Dec (1950)=-40 $^{\circ}$ 57' by Pettersson & Reipurth (1994). The presence of three H II regions, RCW 27, 32 and 33, where signatures of recent low-mass SF have been found by these authors, is one of the peculiarities of this field. In fact, they identified 278 H α -emission objects (with a completeness limit V=19) associated with dark clouds and the three H II regions. In particular, they found two major concentrations, called Vela T1 and Vela T2 T Tauri associations, towards the H II regions RCW 27 and RCW 33, respectively. They took also slit spectra of 24 of the emission-line stars and found that the majority have a spectral appearance similar to T Tauri stars.

Yamaguchi et al. (1999a) attempted to assign a possible age sequence, suggesting that the sparse Vela T1 association, in RCW 27, is more evolved than the tighter Vela T2 association in RCW 33. They explain this sequential SF as an effect of the influence of the exciting OB stars on the molecular clouds.

Massi et al. (1999, 2003) have carried out deep JHK imaging and 1.3 mm continuum photometry of 15 of the Class I sources

found in the VMR D, while Testi et al. (2001) and Massi et al. (2006) have obtained deep JHKs images of six of the most luminous IRAS sources in the VMR D cloud. They found evidences of embedded clusters younger than 1 Myr for which they derived Initial Mass Functions that are consistent with those derived for field stars and clusters.

RCW 32 is likely excited by HD 74804, the brightest star of Collinder 197 (Cr 197). The $H\alpha$ emission stars in this region are very concentrated. It has been the target of a deeper objective prism image and of a ROSAT HRI observation, from which 70 and 30 YSOs, respectively, have been identified. Several embedded sources were found in the region suggesting an age of 1 Myr. The young galactic cluster Cr 197 has been the subject of a dynamical study by Bonatto & Bica (2010), who found it in a super-virial state, with evidence of deviation from dynamical equilibrium.

Several studies, dedicated to individual sources lying in the northern region of the VMR, provide significantly different distances in the range 0.70-1.15 kpc (see Pettersson & Reipurth, 1994, for a review). More recently, a distance of 0.85 kpc has been attributed to the cluster, named ASCC 50, detected in RCW 33, by Kharchenko et al. (2005) and confirmed by Kharchenko et al. (2013).

In this work, we want to study the northern region of the VMR covered by Pettersson & Reipurth (1994) to understand the connection between the star forming sites found in it, and the SF history. In particular, we aim at characterizing and comparing the properties of the three embedded young clusters Vela T2 (corresponding to ASCC 50), Cr 197 and Vela T1, associated with RCW 33, RCW 32 and RCW 27, respectively.

To this aim, we exploit the potential of recently public data as the deep optical- $H\alpha$ VPHAS survey and the available NIR and X-ray data complemented by the new Gaia astrometric and kinematic data. This will allow us to perform a global analysis of the region, by assessing the properties of the three sub-clusters from which to derive hints on the SF process.

The paper is organized as follows. Sect. 2 describes the photometric catalog we assembled and used for this study. In Sect. 3, we describe the selection of accreting YSOs while, in Sect. 4, we describe the selection of YSOs with a circumstellar disk. In Sect. 5, we describe the kinematic analysis of the TGAS Gaia data, while in Sect. 6, we summarize the properties of the members selected with classical methods. In Sect. 7 we illustrate the procedure adopted to identify M-type stars, derive their reddening, and identify M-type giants, MS stars and cluster members. In Sect. 8, we discuss our results on the spatial distribution and the SF history, while our conclusions are summarized in Sect. 9.

2. Catalogue compilation

Figure 1 shows an $H\alpha$ image of $6^\circ \times 6^\circ$ centered at (RA, Dec)=(131°, -41°) taken from the Southern H-Alpha Sky Survey Atlas (Gaustad et al., 2001). It includes the north-western region of the VMR we study here that we label as NW-VMR region. The three areas in the three H II regions RCW 33, RCW 32 and RCW 27, centered, respectively, on RA (J2000)=[132:73,131:2,129:5] deg and Dec (J2000)=[-42:13,-41:3,-40:6] will be the subject of this work.

The NW-VMR is included in the VST Photometric $H\alpha$ Survey of the Southern Galactic Plane (VPHAS+ Drew et al., 2014). We used photometry of Data Release 2 (Date: 2015-07-30) from the ESO Catalogue Facility within a radius of 3° around (RA, Dec)=(131°, -41°). This multi-band source catalog has been obtained from observations of the OmegaCAM

CCD imager mounted on the 2.6 m VLT Survey Telescope (VST) on Cerro Paranal, Chile. Imaging is performed with the IMAGE/OFFSET technique by using the bands u_SDSS, g_SDSS, r_SDSS, i_SDSS, NB_659, corresponding to the five filters u , g , r , i and $H\alpha$, down to $r \sim 21$.

From this catalog, we selected objects tagged as the best available detections per unique object, with signal-to-noise ratio > 10 and a DAOPHOT (Stetson, 1987) point spread function fitting score of $CHI < 1.5$ in the r , i and $H\alpha$ bands. With this selection, the VPHAS+ catalog in NW-VMR includes 499 664 objects with photometric errors smaller than 0.1 mag. Since the observations with the u and g filters cover only the northwestern part of RCW 27, we did not consider in this work the u and g magnitudes.

VPHAS magnitudes are given both in the Vega and AB system (Oke & Gunn, 1983). A detailed description of the survey strategy, photometric offsets, photometric quality, exposure times and pipeline used to derive the magnitudes can be found in Drew et al. (2014).

The deep VPHAS+ photometric catalog ranges from $g=13$ down to $g \sim 21$. Magnitudes $g < 13$ are affected by saturation (Drew et al., 2014). For this reason, we compiled the photometric catalog of the NW-VMR region by using the VPHAS+ catalog for $r \geq 13$ and the AAVSO¹ Photometric All-Sky Survey (APASS) DR9 (Henden et al., 2016) catalog for $r < 13$. To check the VPHAS+ calibration, we cross-matched the APASS magnitudes, calibrated in the SDSS² AB system, with the VPHAS+ catalog by considering objects with $14 < r < 17$, both in the VPHAS+ and APASS catalog. These limits have been chosen to avoid saturated objects in the VPHAS+ catalog and large errors in the APASS catalog whose limiting magnitude is about $r=17.8$ mag. By using a matching radius of $1''$, we computed the systematic shift between the astrometric systems of the two catalogs corresponding to $RA_{VPHAS} - RA_{APASS} = 0'.07$ and $Dec_{VPHAS} - Dec_{APASS} = 0'.05$. We corrected the APASS coordinates for this shift and cross-correlated again the two catalogs by adopting a matching radius of $0'.5$. The 5 982 objects common to VPHAS+ and APASS catalogs were used to check the VPHAS+ photometry. By considering the range $0.2 < r - i < 1.5$, comprising the bulk of objects of our interest, we find that the r and i magnitude differences between VPHAS+ and APASS catalogs do not show any dependence on the relevant colors, while the median offsets are 0.009 and -0.020 mag, respectively in the i and r bands. Since these are negligible with respect to the photometric errors, we do not apply any correction to the magnitudes. The final optical catalog includes 568 811 entries in NW-VMR.

The NIR counterparts of the objects included in our optical catalog were found in the 2MASS Point Sources catalog (Cutri et al., 2003) from which we selected only objects with photometric quality flag 'A' in at least one of the three magnitudes JHK. The cross-match between the two catalogs has been performed by using the match service available at CDS, Strasbourg. By adopting a matching radius of $1''$, we found that 431 860 of the 568 811 entries in our catalog have at least one counterpart in the 2MASS catalog.

The field we are studying has been also included in the Vela-Carina Spitzer IRAC program, an extension program of the Galactic Legacy Infrared Midplane Survey Extraordinaire (GLIMPSE, Benjamin et al., 2003; Churchwell et al., 2009). We used the Vela-Carina Catalog (Zasowski et al., 2009), that in NW-VMR includes 170 206 objects with IRAC/Spitzer mag-

¹ American Association of Variable Star Observers.

² Sloan Digital Sky Survey

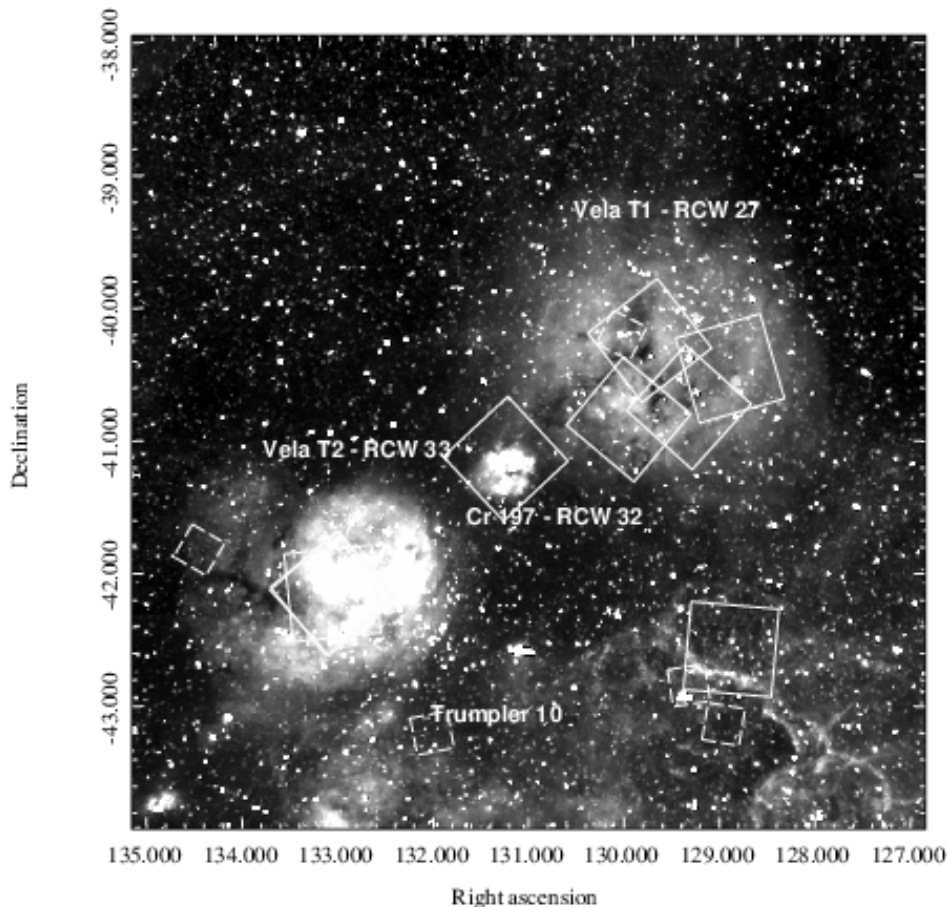


Fig. 1. A $6^\circ \times 6^\circ$ $H\alpha$ image, centered on (RA, Dec)=(131, -41), taken from the Southern H-Alpha Sky Survey Atlas (Gaustad et al., 2001). The positions of Trumpler 10 and of the three H II regions are indicated. The field of view (FOV) of the ROSAT HRI and Chandra ACIS-I observations are indicated by solid and dashed boxes, respectively.

nitudes. We cross-matched the list of IRAC sources with our catalog by adopting a matching radius of $0''.5$ and found that 89 263 IRAC sources have a counterpart in our optical catalog³.

In addition, we used the TGAS subset of the *Gaia* DR1 catalog (Gaia Collaboration et al., 2016a,b), limited to the objects included in the Hipparcos and Tycho-2 Catalogues, for which we have positions, proper motions (PM) and parallaxes. The TGAS catalog was cross-matched⁴ with the APASS catalog in NW-VMR, finding 3 065 matches within $1''$.

In NW-VMR several X-ray sources were also found from the ROSAT High Resolution Imager (HRI, 1RXH, 3rd Release) and from the Chandra ACIS observations taken from the Chandra Data Archive (Wang et al., 2016). The FOV of these observations are shown in Fig. 1. We cross-matched the two X-ray catalogs, including 25 Chandra and 75 ROSAT sources (with 3 sources in common to the two catalogs), with our optical catalog by using the match service provided by CDS, and adopting a radius of $5''$. Within the NW-VMR area considered here, we considered the optical counterparts closest to the 97 X-ray sources as YSOs.

In particular, we have 8 and 34 X-ray sources from the ROSAT catalog falling, respectively, in RCW 33 and RCW 32,

and 40 X-ray sources in RCW 27, of which 36 from the ROSAT catalog and 7 from the Chandra ACIS catalog, with 3 objects detected with both Chandra and ROSAT. The very small number of X-ray detections is due to the limited ROSAT sensitivity and to the small exposure times (from 1 to 46 ks) and coverage of the Chandra observations in this region.

3. Candidate young stars with ongoing accretion from $H\alpha$ excesses

CTTS stars are YSOs with ages younger than few Myrs, characterized by a circumstellar disk that transfers its matter onto the central star. This process involves high velocities of the gas impacting on the star with a subsequent formation of a surface shock emitting predominantly in the UV, while $H\alpha$ emission is produced in the accretion funnel. The first gives rise to the UV flux excess distinctive of CTTS, while the second can be photometrically detected through the $(r-H\alpha)$ color, that is a measurement of the strength of the $H\alpha$ emission line relative to the photospheric continuum in the r band.

Figure 2 shows the $r-H\alpha$ vs. $r-i$ color-color diagram (CCD), for all 473 998 VPHAS+ objects in NW-VMR region with color errors < 0.1 mag. The synthetic unreddened main sequence for stars with spectral type from O6V to M2V and the giant locus

³ the GLIMPSE point source accuracy is typically 0.3 arcsec

⁴ Using the match service provided by CDS, Strasbourg

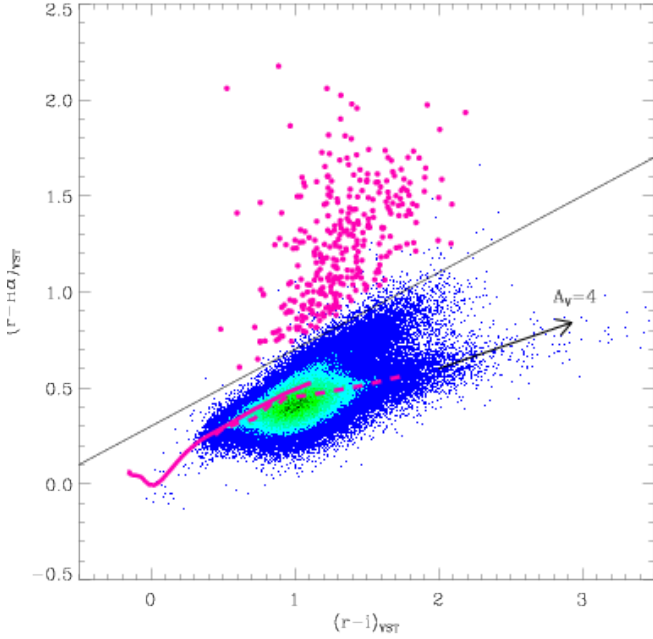


Fig. 2. VST $r\text{-H}\alpha$ vs. $r\text{-i}$ diagram plotted as a two-dimensional stellar-density histogram using a binning of 0.005×0.005 and a 8 level colour-coded scale such that high source densities (130 per bin) are dark-green and the lowest densities (one per bin) are violet. The magenta solid and dashed lines are, respectively, the synthetic unreddened main sequence and giant loci given by Drew et al. (2014), while the black solid line is the limit adopted to select objects with $\text{H}\alpha$ excesses, drawn as magenta circles.

for stars with spectral type from K0III to M5III, computed by Drew et al. (2014), are also shown. Since the NW-VMR region includes a very large area with patterns of dark obscuring matter, spatially variable reddening is expected. This explains the large spread in colors around the synthetic loci. Nevertheless, the bulk of main sequence and giant stars are enclosed within the blue region, while objects with larger $r\text{-H}\alpha$ are stars with $\text{H}\alpha$ emission lines. We thus consider as stars with $\text{H}\alpha$ excesses those with $r\text{-H}\alpha$ color larger (with at least 5σ confidence) than the limit $r\text{-H}\alpha = 0.3 + 0.4 \times (r\text{-i})$. In this way we select 329 CTTS candidates.

Figure 3 shows the spatial distribution of VPHAS+ objects in the NW-VMR region. Even though not the whole region is covered by VPHAS+ observations, the three H II regions we study are completely covered, except for the north part of RCW 27. The 329 objects selected as $\text{H}\alpha$ emission line stars are overplotted and clearly show a peculiar pattern with a tight concentration in RCW 32, a round but quite sparse distribution in RCW 27 and an elongated concentration in the RCW 33 region. This distribution is very similar to that found for the $\text{H}\alpha$ -emitting stars by Pettersson & Reipurth (1994).

In order to understand the nature of the selected objects, we plotted them in the r vs. $r\text{-i}$ diagram shown in Fig. 4. Most of the selected objects are on the red side of the diagram and are consistent with a low mass population of PMS stars, with ages younger than 10 Myr, as derived from the comparison with the PISA 10 Myr isochrone (Tognelli et al., 2011; Randich et al., 2017), assuming a distance of 750 pc and reddening $E(B\text{-}V) = 0.2$ (see Section 5). These results strongly suggest the presence of

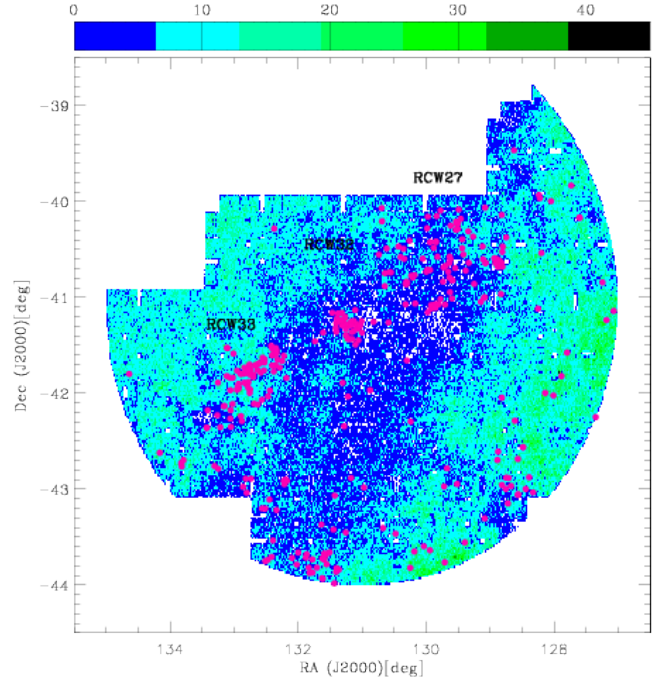


Fig. 3. Spatial distribution of the VPHAS+ stars in the NW-VMR region, plotted as a two-dimensional stellar-density histogram using a binning of $0'.02 \times 0'.02$ and a 7 level colour-coded scale such that high source densities (45 per bin) are dark-green and the lowest densities (one per bin) are blue. Objects with $\text{H}\alpha$ excesses are drawn as magenta circles.

three young clusters with different spatial distributions associated to the H II regions RCW 33, RCW 32 and RCW 27, respectively.

4. Candidate disk-bearing young stars from NIR excesses

The presence of NIR excesses with respect to photospheric stellar colors is a very efficient tool to select YSOs. Several optical/NIR colors can be used to select objects with evident NIR excesses due to the presence of a circumstellar dusty disk in YSOs. Spitzer/IRAC CCDs are a powerful method to distinguish YSOs with disk from old stars, since IR excesses in these colors do not follow the reddening direction and can therefore be easily separated from reddened objects. The $[3.6]\text{-}[4.5]$ vs. $[5.8]\text{-}[8.0]$ diagram in Fig. 5 includes all the objects with error smaller than 0.2 mag and with $\text{S/N} > 10$ in all four bands, as done in Zasowski et al. (2009) for data from the same survey. By using the conditions given in Gutermuth et al. (2009), that involves all IRAC/Spitzer magnitudes, we selected 461 candidate Class II, i.e. disk-bearing objects and 20 Class I YSOs, i.e. YSOs still surrounded by infalling material from which they form.

We also looked for possible contaminants (AGN or PAH galaxies) by following the definitions given in Gutermuth et al. (2009). We found that our sample of Class II YSOs includes 15 sources that are likely PAH contaminants and we removed them from our sample.

Warm disks can show IR excesses in the K and H bands but also in the J band and, in fact, the J-H vs. H-K diagram is usually considered to select Class II stars (Meyer et al., 1997; Cieza et al., 2005). However, in this diagram it is very difficult to dis-

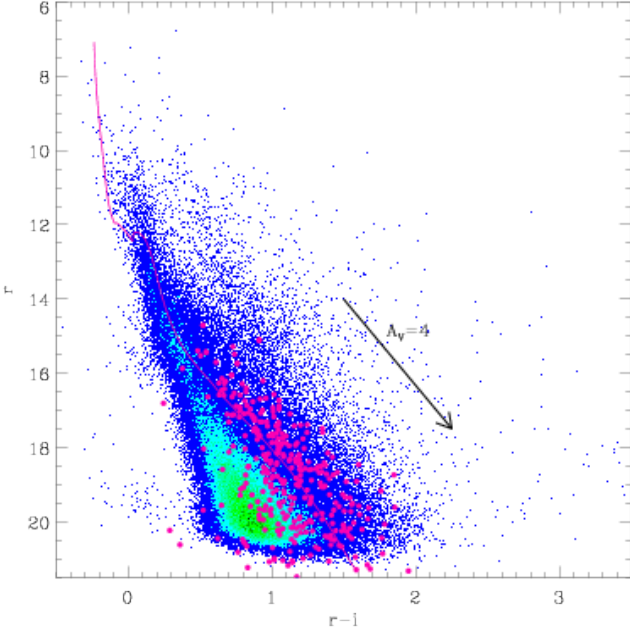


Fig. 4. SDSS r vs. $r-i$ diagram plotted as a two-dimensional stellar-density histogram using a binning of 0.01×0.01 and a 7 level colour-coded scale such that high source densities (70 per bin) are dark-green and the lowest densities (one per bin) are blue. The magenta solid line is the 10 Myr PISA isochrone, assuming a distance of 750 pc and $E(B-V)=0.2$. Objects with $H\alpha$ excesses are drawn as magenta circles.

Table 1. Relations for a G2V star using the Cardelli et al. (1989) and O’Donnell (1994) extinction curve with $R_V=3.1$ in the SDSS ugriz and 2MASS photometric systems (Marigo et al., 2017).

$\frac{A(u)}{A(V)}$	$\frac{A(g)}{A(V)}$	$\frac{A(r)}{A(V)}$	$\frac{A(i)}{A(V)}$	$\frac{A(z)}{A(V)}$	$\frac{A(J)}{A(V)}$	$\frac{A(H)}{A(V)}$	$\frac{A(K_s)}{A(V)}$
1.569	1.206	0.871	0.683	0.492	0.294	0.181	0.118

tinguish reddened objects from NIR excesses, since the region consistent with Class II stars overlaps with that of reddened objects, and therefore only objects with very strong NIR excesses can be selected from this diagram. On the contrary, objects with excesses in the H or K bands can be very well discriminated from reddened objects if the diagram involves an optical color, dominated by photospheric emission even in Class II stars. For example, as discussed in Damiani et al. (2017), in the $r-i$ vs. J-H and/or $r-i$ vs. H-K diagrams, objects with excesses in the H-K or J-H colors can be confidently found on the red side of the main locus of normal reddened stars.

Figures 6, 7 and 8 show the $r-i$ vs. H-K, the $r-i$ vs. J-H and the J-H vs. H-K diagrams of all objects with error in $r-i$, H-K and J-H smaller than 0.1. It is evident that the bulk of the objects, mostly including giants and MS stars, follows the reddening vector. In this work we adopted the relations of the extinction curve with $R_V=3.1$ given in Table 1.

The comparison of the data with the 10 and 100 Myr isochrones suggests that the tail of objects in Fig.7 with J-H around 0.6 and $r-i \gtrsim 1$ is the locus of M-type stars, while objects on the right of the dashed lines in the first two diagrams can be considered candidate YSOs. There are in total 221 YSOs

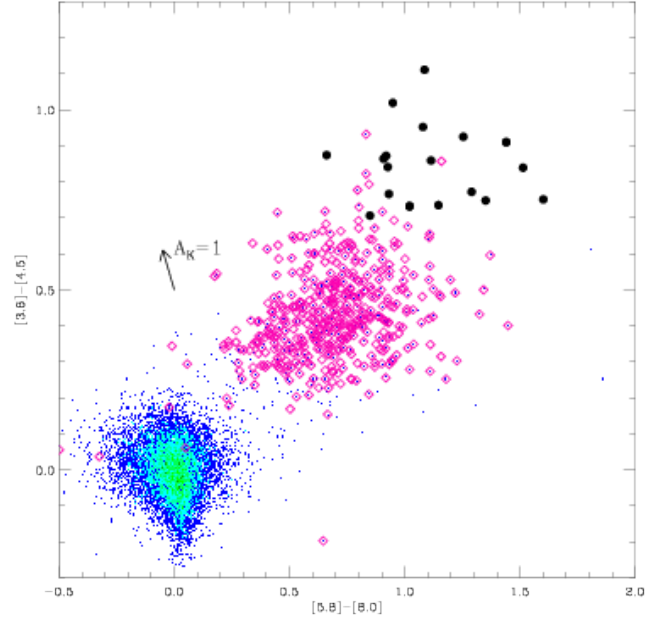


Fig. 5. $[3.6]-[4.5]$ vs. $[5.8]-[8.0]$ diagram plotted as a two-dimensional stellar-density histogram using a binning of 0.01×0.01 and a 7 level colour-coded scale such that high source densities (29 per bin) are dark-green and the lowest densities (one per bin) are blue. Class II stars are drawn as magenta diamonds while Class I objects are indicated by black points. Reddening vector for $A_K=1$ based on the extinction law in the direction of RCW 49 of Indebetouw et al. (2005) is shown as a filled arrow.

showing excesses both in the J-H and H-K colors. Among them, 111 were selected as YSOs with disk also using the IRAC data, while the remaining 110 lie outside the region covered by the IRAC/Spitzer observations. This finding is fully consistent with the observation coverage.

To include also the objects that lack detections in the less sensitive 5.8 and $8.0 \mu\text{m}$ bands, or with small excess in the J band, we selected 296 additional YSOs by taking objects with excess in the H-K color and that fulfill at least one of the previous three conditions involving the IRAC colors $[3.6]-[4.5]$, $[3.6]-[5.8]$ and $[4.5]-[8.0]$. Finally, to include possible YSOs with a small excess in the K band, we selected another 125 YSOs, with excess in J-H and in at least one of the IRAC colors. At the end, we have a total of 559 Class II YSOs, included in at least one of the samples selected as described above, plus 20 Class I YSOs that are shown in Fig. 9, where the area covered by IRAC/Spitzer observations is also shown. The spatial distribution of the Class II and I stars is very similar to that found in the previous section for CTTS and, again, confirms the presence of three embedded young clusters in NW-VMR. The circular boundaries shown in the figure trace the locations of the dusty shells/bubbles that surround the three H II regions, as can be seen, on the WISE image of the region (see Fig. 22).

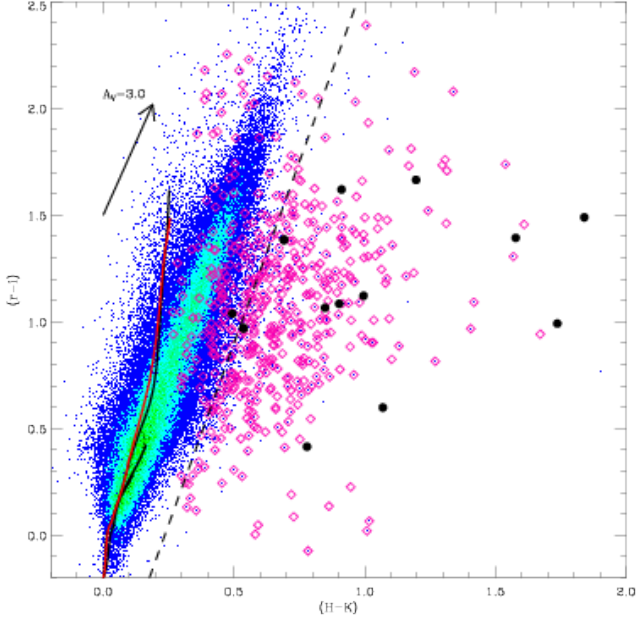


Fig. 6. $r-i$ vs. $H-K$ diagram plotted as a two-dimensional stellar-density histogram using a binning of 0.01×0.01 and a 7 level colour-coded scale such that high source densities (54 per bin) are dark-green and the lowest densities (one per bin) are blue. Symbols are as in Fig. 5. The black and red solid lines are the 100 and 10 Myr PISA isochrones. The reddening vector is also shown.

5. Kinematic populations

5.1. The Trumpler 10 association

Even if limited to very bright stars, Gaia TGAS data give us the opportunity to study the kinematics across large fields. In order to understand if the three young populations belong to the same molecular cloud and share a similar motion, we compared their PMs and parallaxes. As already known in the literature, the VMR is behind the intermediate age OB association Trumpler 10 (RA=131°872, Dec=-42°40) of which 23 members, 22 B-type and one A0V star are known (de Zeeuw et al., 1999; Kharchenko et al., 2013).

The distance of Trumpler 10 has been estimated by several authors: 417 pc (Kharchenko et al., 2013), 424 pc (Dias et al., 2002), 366 ± 23 pc (de Zeeuw et al., 1999). Located at a galactocentric distance of $R_{GC} = 8.1$ kpc, it suffers from a relatively low reddening, $E(B-V) = 0.029$ (Kharchenko et al., 2013). The most recent values for the cluster age are 24 Myr (Kharchenko et al., 2013), ~ 35 Myr (Dias et al., 2002) and 15 Myr (de Zeeuw et al., 1999).

Since our field includes this association, we first studied the PM and parallax distributions around its center, as shown in Fig. 10. To detect a population sharing the same motion and with a common parallax, we adopted the following procedure: we computed the maximum of a bidimensional array of PMs in RA and Dec, assuming a PM bin of 1 mas/yr both in μ_α and μ_δ in the range $-20 < \mu_\alpha/\text{mas yr}^{-1} < 20$ and $-20 < \mu_\delta/\text{mas yr}^{-1} < 20$ and in parallax steps of $\Delta\pi=1$ mas. This large π step is chosen to account for the large errors on the parallax values of the TGAS GAIA data. To avoid a binning dependence,

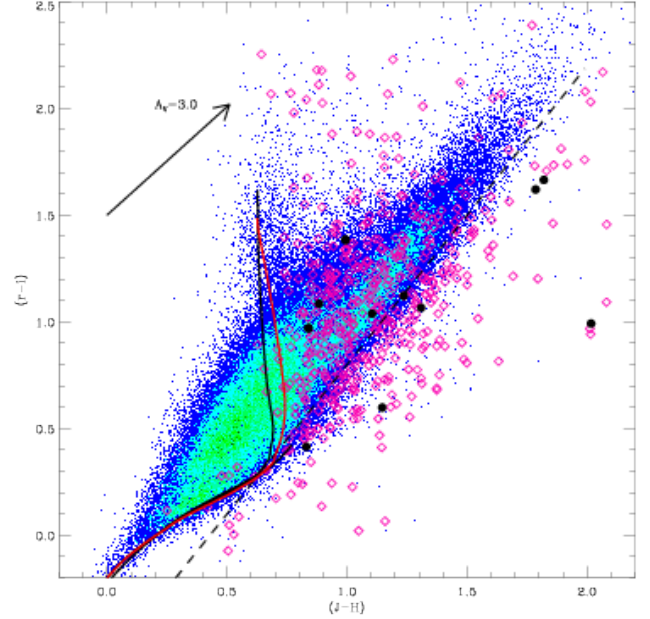


Fig. 7. $r-i$ vs. $J-H$ diagram plotted as a two-dimensional stellar-density histogram using a binning of 0.01×0.01 and a 7 level colour-coded scale such that high source densities (39 per bin) are dark-green and the lowest densities (one per bin) are blue. Symbols are as in Fig. 5.

we repeated the computation by shifting by 0.1 mas the parallax bin while exploring the parallax range $0 < \pi/\text{mas} < 4$, (corresponding to distances larger than 250 pc) where most of the objects are distributed. The maximum value of each array represents the tridimensional condition to detect clusters of objects at the same distance sharing the same motion. For each parallax bin, we considered the μ_α and μ_δ corresponding to the maximum of the array and therefore we selected all the objects with $\sqrt{(\mu_\alpha)^2 + (\mu_\delta)^2} < 2$ mas. If the number of objects within this 3-d region is larger than 10, then the corresponding μ_α , μ_δ and π are associated with a population⁵. As expected, we obtained similar values for close parallax ranges and therefore we considered as final parameters for a population, the median values associated with the selected maxima.

To detect the population of Trumpler 10, we considered the whole TGAS catalog in the entire region we are studying, because this association is known to be very dispersed on the sky. In this region, our procedure enabled us to detect a main population, at $\pi = 2.37$ mas, corresponding to 422 ± 32 pc (1σ uncertainty). We conclude that this latter population is the one associated with Trumpler 10 and includes 63 objects.

Figure 10 shows also the spatial distribution of the TGAS stars found in this region, where the population of Trumpler 10 (blue symbols) is well distinct from the others (see below) for its kinematic parameters, while its spatial distribution is very dispersed throughout the region, confirming the de Zeeuw et al. (1999) results. The color-magnitude diagram (CMD) of these objects is shown in Fig. 11 and compared with the PISA isochrone with the parameters indicated in the Figure. The se-

⁵ the adopted threshold corresponds to about 3σ of the distribution of objects where no hint of clustering is found

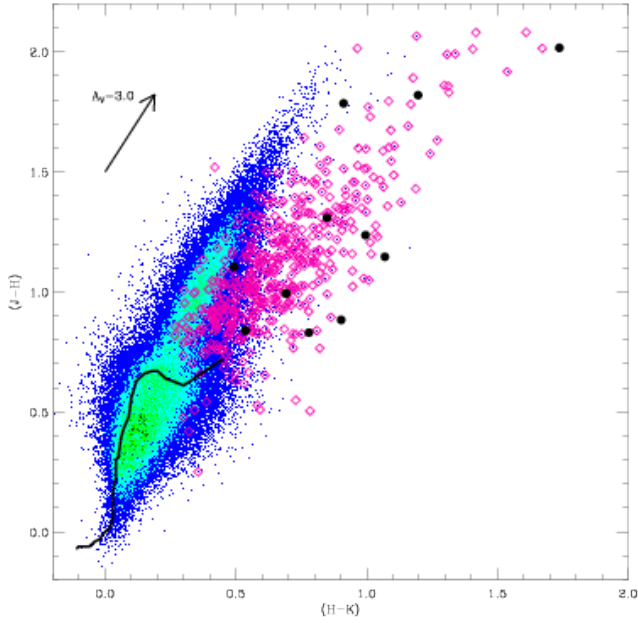


Fig. 8. J-H vs. H-K diagram plotted as a two-dimensional stellar-density histogram using a binning of 0.01×0.01 and a 7 level colour-coded scale such that high source densities (56 per bin) are dark-green and the lowest densities (one per bin) are blue. Symbols are as in Fig. 5. The black solid line is the MS locus (Kenyon & Hartmann, 1995).

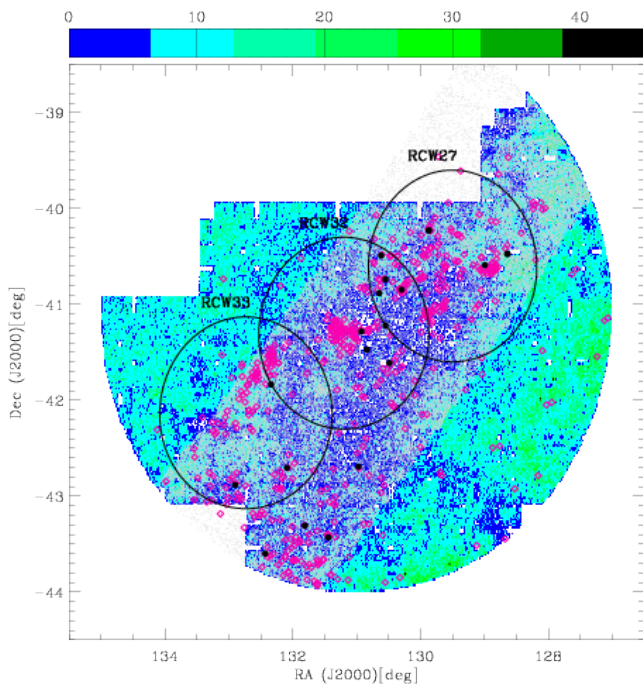


Fig. 9. Spatial distribution as in Fig. 3 where all the Spitzer/IRAC sources are overplotted with grey symbols. YOSs with IR excesses are indicated as in Fig. 5. The three circular boundaries delimit the regions of the three clusters.

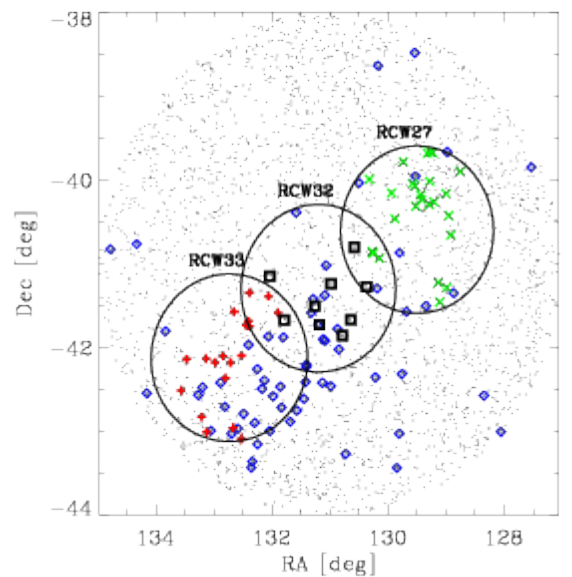
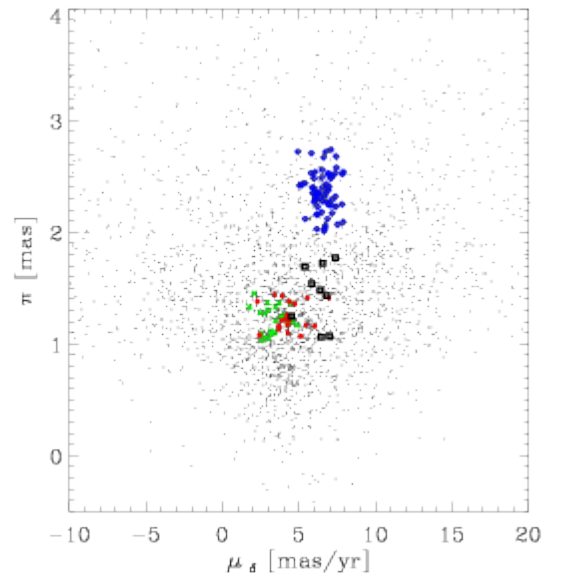
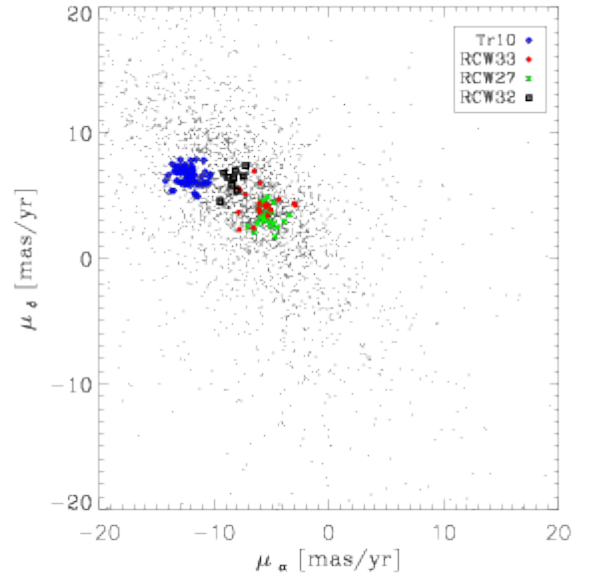


Fig. 10. μ_α vs. μ_δ (upper panel), π vs. μ_δ (middle panel) and spatial distribution (lower panel) of the TGAS catalog in the region of the VMR studied here. Blue diamonds are associated with the Trumpler 10 cluster, red plus are associated with YOSs in the RCW 33 region, green X are associated with YOSs in the RCW 27 region and black squares are associated with YOSs in the RCW 32 region.

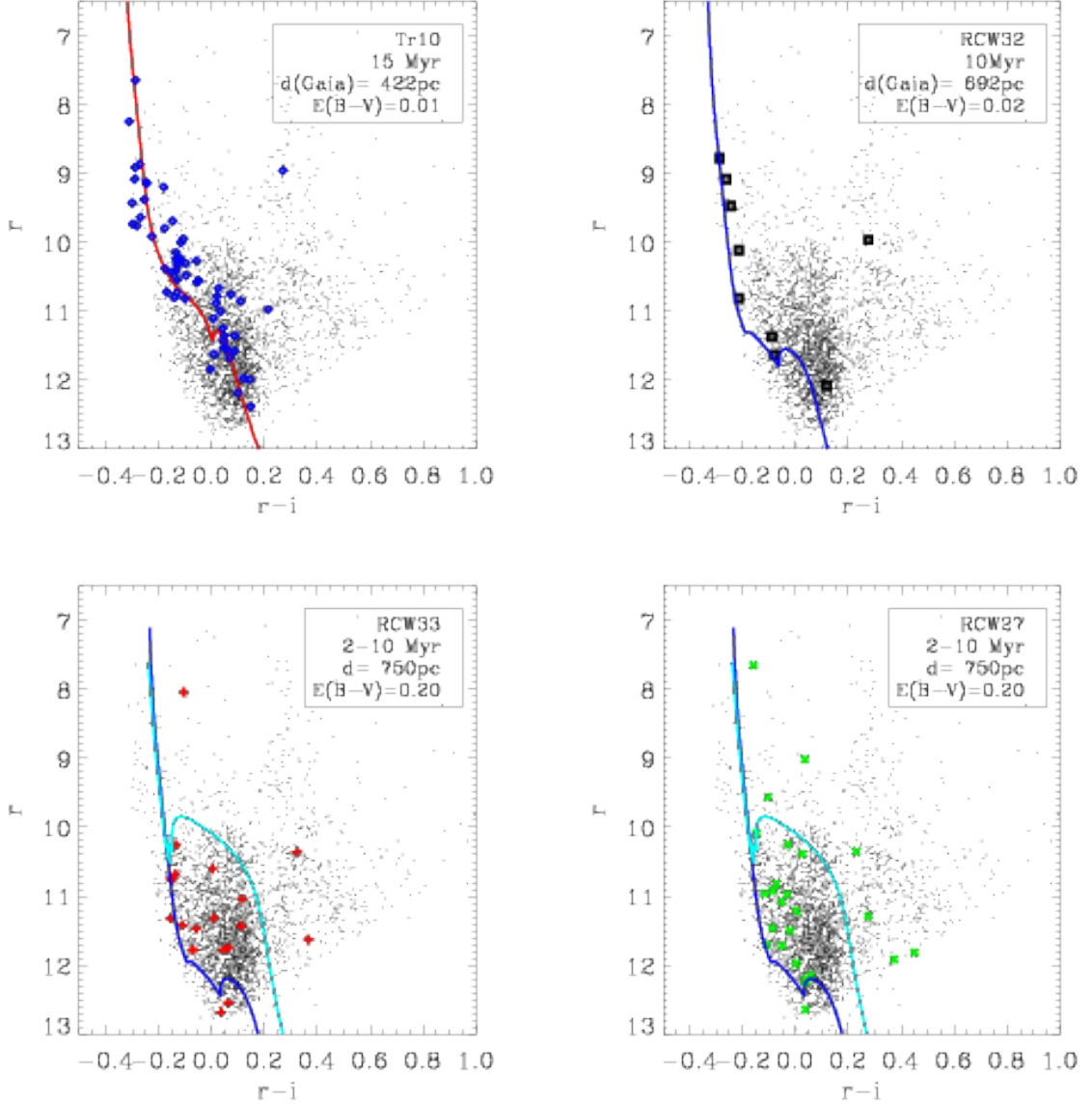


Fig. 11. r vs. $r-i$ diagrams of the cluster Trumpler 10 and of the three regions centered on RCW 33, RCW 27 and RCW 32. Coloured symbols are as in Fig. 10 and indicate the candidate members for each region, selected kinematically by using Gaia data.

quence shows a spread around the isochrone. A thorough assessment of the nature of this spread, which would require detailed investigation of the entire population of the association, is beyond the aim of this work.

5.2. The cluster Cr 197 and RCW 32

The analysis of PMs and parallaxes in the region of RCW 32, corresponding to the cluster Cr 197, has been performed as done for Trumpler 10. This last association is spread across a large region overlapping that of Cr 197. For the kinematic analysis of Cr 197, we used only the TGAS data within a radius of $45'$ from its center. This radius has been chosen to avoid the two neighbouring regions RCW 33 and RCW 27, that show a more dispersed spatial distribution. In addition, we discarded objects with $\mu_\alpha < -10$ mas/yr and $\pi > 2$ mas, since they are associated with Trumpler 10. Our procedure enabled us to detect two groups of objects in the PM plane, lying in the same parallax range. The

two populations do not show a peculiar spatial distribution, being both quite sparsely distributed, but their distribution in the CMD suggests that the group of objects corresponding to $(\mu_\alpha, \mu_\delta) = (-8.3, 5.8)$ mas/yr in the parallax range $1.0 < \pi < 2.0$ (indicated with black squares in Fig. 10) can be associated with the cluster Cr 197. The mean parallax of these objects is 1.44 mas, which corresponds to a distance of 692 ± 128 pc. Indeed, the 9 selected objects (black squares in Fig. 10 and 11) follow quite well the 10 Myr PISA isochrone, at a distance of 692 ± 80 pc ($\pi = 1.45$), assuming $E(B-V) = 0.02$, as shown in Fig. 11. Our analysis therefore suggests a cluster distance significantly smaller than that found by Bonatto & Bica (2010), namely 1050 ± 200 pc, based on near-infrared photometry and a statistical field star decontamination. Our value is, instead, consistent with the distance of ≈ 700 pc derived by Georgelin et al. (1973) and Crampton & Fisher (1974). In addition, the r vs. $r-i$ diagram suggests that the cluster is less reddened than the value reported in the literature, equal to $E(B-V) = 0.34$ (Bonatto & Bica, 2010).

5.3. The cluster Vela T2 and RCW 33

As done in the previous sections, we performed the PM and parallax analysis also in the RCW 33 region. Even in this case, there is a strong contamination from the Trumpler 10 members and therefore we discarded objects with $\mu_\alpha < -10$ mas/yr and $\pi > 2$ mas. After that, the diagram (μ_α, μ_δ) shows a group of objects with a quite elongated distribution in the μ_α axis. This includes two groups that are distinguishable in the parallax diagram, in the range $0.5 < \pi/\text{mas} < 1.0$ and $1.0 < \pi/\text{mas} < 1.5$. The second subgroup, corresponding to a distance of about 800 pc, is centered to $(\mu_\alpha, \mu_\delta) = (-5.57, 4.10)$ mas/yr (red symbols in Fig. 10 and 11). This population includes 19 objects with an elongated spatial distribution similar to the YSOs selected above. In the CMD, these objects lie in a region compatible with both MS and PMS stars (Fig. 11). We associate this group of stars to the cluster Vela T2.

5.4. The cluster Vela T1 and RCW 27

The PM analysis of the objects in RCW 27 shows a well distinct clump in the (μ_α, μ_δ) diagram for $\pi > 1.0$ mas at $(\mu_\alpha, \mu_\delta) = (-5.48, 3.39)$ mas/yr. The population, corresponding to RCW 27 has been selected by taking objects with PMs within 2 mas/yr from this peak and with $1.0 < \pi < 1.5$ mas. This population includes 25 objects that mainly lie in the north-western part of RCW 27 (green symbols in Fig. 10 and 11). The CMD of the selected objects is consistent with a PMS population located at about 750 pc, with age less than 10 Myr.

6. Summary of "classical" YSO selection

We summarise here the properties of candidate YSOs found in the NW-VMR including all the objects with H α or NIR excesses, selected as described in Sect. 3 and 4, with a X-ray detection, or with PMs and parallaxes consistent with the populations in RCW 33, RCW 32 or RCW 27, selected as described in Sect. 5.

We selected a total of 907 candidate YSOs in the whole area. Those included in the circular regions with radius 1 deg in RCW 33, RCW 32 and RCW 27, are 210, 177 and 288, respectively. Note that the YSOs falling in the overlapping areas were associated to the external ones, i.e. RCW 33 and RCW 27. We will refer to the 907 objects as members selected with *classical* methods. Optical/NIR photometry and the membership information of the selected YSOs are given in Table 2.

We note that the list is not complete since the spatial coverage of data used to select them is incomplete. The spatial distribution of all the objects selected as YSOs is shown in Figure 12. We omitted from Figure 12 the 63 kinematic objects candidate members of Trumpler 10 since they are not related to the young populations we are investigating in this work.

As already discussed, many of the selected YSOs define three young clusters associated to the three H II regions. However, there is an additional stellar sub-cluster located right to the south of RCW 33, corresponding to Vela-D, and composed of mainly H α and IR-excess YSO candidates. This region has been the subject of a Balloon-borne Large-Aperture Submillimeter Telescope (BLAST) survey by Olmi et al. (2009) where 141 pre-stellar and protostellar sources have been found. The presence of YSOs objects detected also in the optical and NIR bands and the strong spatial correlation of these YSOs with the cores found in Olmi et al. (2009) is a further confirmation of the ongoing star formation in this region, characterised by the lack of massive O-type stars.

We note the presence of an additional group of X-ray sources located to the east of RCW 33. These objects are located in a region devoid of YSOs selected in this work, and on the boundary of the field and thus we are not able to assert if this group of objects is associated to a young sub-cluster.

The three circular areas in the H II regions are those with the best coverage but, for example, the northern region of RCW 27 lacks VPHAS+ data and the northern regions of RCW 33 and RCW 32 lack SPITZER/IRAC data. For this reason, we will avoid any analysis requiring completeness of the samples. The YSOs with evidence of accretion from H α and of circumstellar disk from the IR are 136. The objects with NIR excess, selected also with PMs and parallax, are 3, while no objects, selected kinematically, show evidence of accretion or X-ray emission. Most of the candidate YSOs have only one youth indicator and this suggests that the methods are complementary.

We find that members selected as YSOs with NIR, H α excess and X-rays show a similar spatial distribution in each of the 3 H II regions, even though the X-ray sample is very limited regarding both spatial coverage and duration of observations. The members selected using Gaia data, expected to be the more massive ones, show a spatial distribution similar to that of the other members in Vela T2 and T1, while in Cr 197, they are poorly correlated with the other member positions. This could be due to the lower performance of Gaia data in very crowded regions, as the cluster Cr 197 in RCW 32 or to source extinction. In fact, the TGAS sample mainly includes lightly absorbed stars. Since the region harbors a large number of spatially clustered disk-bearing YSOs, clouds and a nebular background, a spatially varying source extinction is expected, that could explain the poor correlation with Gaia members.

In conclusion, we find that the whole region includes different sites of ongoing or recent SF. We will concentrate our attention on the three areas of the H II regions, whose properties will be studied in the following sections.

7. Features of M-type stars

The region studied in this work lies on the galactic plane and therefore includes a large number of field stars. Due to the presence of the molecular clouds, the background objects are expected to be very reddened, while those in front of the nebula are likely affected by small reddening. In general, in the optical and NIR CCD and CMD, foreground and background field stars cannot be distinguished from YSOs, since the color distribution of all these objects follows the direction of the reddening vector. Nevertheless, using appropriate combinations of optical and NIR magnitudes, the color distribution of M-type stars does not follow the reddening vector and this property can be used to select M-type stars, as recently discussed in Damiani (2018) and Venuti (2018, in preparation).

This is clearly visible in the r-i vs. i-J, i-H and i-K diagrams shown in Fig. 13, where the comparison with the theoretical loci of PMS, MS and giant stars shows that the region of M-type stars ($r-i \gtrsim 0.75$) is clearly distinguishable from that of hotter, reddened stars. In particular, the bulk of our data in the M-type range is compatible with stars affected by very small reddening, while all objects on the red side of the diagram are very reddened stars.

Following the position of the theoretical loci in the three diagrams, compared to the bulk of objects that lie along the reddening vectors, we select as M-type stars all the objects with r-i larger than the limits indicated by the solid green lines in all the three diagrams, and with i-K > 2.2. The simultaneous use of the three diagrams allows us to select a sample of M-type stars that

Table 2. Optical/NIR photometry and membership criteria of YSOs selected with *classical* methods. M1, M2, M3, M4 and M5 stand for membership from $H\alpha$, u, IR excesses, kinematics and X-ray detection, respectively; 1 indicates member while 0 indicates non-member. Full table available in electronic format only.

CNAME	RA (J2000)	Dec (J2000)	u	g	r	i	$H\alpha$	J	H	K	M1	M2	M3	M4	M5
08442605-4105159	131.10853	-41.08775	11.43	11.22	...	10.19	9.80	9.69	0	0	0	0	1
08435467-4114538	130.97779	-41.24827	9.46	9.71	...	9.33	9.35	9.30	0	0	0	1	0
08441101-4116189	131.04588	-41.27192	11.65	11.20	...	10.22	0	0	0	0	1
08443774-4115371	131.15724	-41.26032	14.75	14.11	0	0	0	0	1
08444029-4116378	131.16788	-41.27716	7.24	7.23	...	6.39	6.25	6.24	0	0	0	0	1
08451790-4112462	131.32456	-41.21283	14.90	14.27	0	0	0	0	1
08444546-4117322	131.18942	-41.29228	14.57	13.94	0	0	0	0	1
08451500-4117349	131.31251	-41.29301	12.19	12.05	...	11.20	10.93	10.87	0	0	0	0	1
08450273-4123123	131.26138	-41.38674	15.67	15.13	0	0	0	0	1
08445256-4124287	131.21902	-41.40797	8.78	8.71	...	7.83	7.55	7.48	0	0	0	0	1
08411684-4050026	130.32015	-40.83406	11.22	11.09	...	10.11	9.69	9.37	0	0	1	0	0

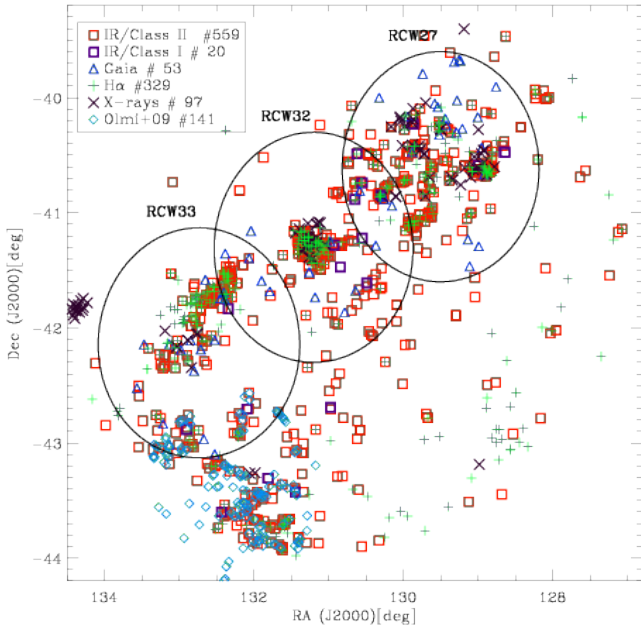


Fig. 12. Spatial distribution of all candidate YSOs, selected with different membership *classical* criteria, plotted with different symbols. Cyan diamonds are the 141 sub-mm cores found with the BLAST survey by Olmi et al. (2009). The three circles of l' in radius delimit the regions around the three clusters.

is as clean as possible. In the three diagrams, YSOs selected with *classical* methods mainly lie in the region of reddened stars and only a small fraction of them fall in the region of M-type stars. As expected, the spread of the selected YSOs in the r - i vs. i -K diagram is larger than that in the r - i vs. i -J diagram, since this sample includes stars with IR excesses, mainly in the K band. Therefore, it could include also M-type stars with disk or accretion, that, due to the presence of IR excesses, fall outside of the region of M-type stars.

A further feature of the M-type stars is that in the r - i vs. i -J diagram the theoretical loci of PMS, MS and giant stars almost overlap, while in the r - i vs. i -H and r - i vs. i -K diagrams they are quite separated. This occurs because both i -H and i -K colors of giant M stars of a given temperature are redder than those of MS

stars as is clearly evident in Fig. 14, where the stellar gravities, for a set of theoretical PISA isochrones at solar metallicity, are shown as a function of the i -J and i -K colors, respectively. This feature implies that the i -H and i -K colors of the PMS isochrones of ages $\gtrsim 10$ Myr are similar to MS star colors, while for the very young PMS stars (0.5 Myr in the case of our models) the i -H and i -K colors are more similar to those of the giant locus, as shown in Fig. 15.

In the r - i vs. i -H and i -K diagrams, PMS isochrones with ages from 0.5 to 5 Myr are located between the giant and the MS loci. Therefore the PISA models predict that the i -H and i -K colors are sensitive to the stellar ages and gravities, at least for $\text{Log } g > 3.0$. M-type giants, being very low gravity objects ($\text{Log } g < 3.0$), have i -H and i -K colors more similar to YSOs (< 1 Myr) rather than to objects with ages > 5 -10 Myr. Therefore, within the limits of the photometric errors, at a given temperature (or analogously at a given r - i color), the i -H and i -K colors can be exploited to constrain also the luminosity class of M-type stars, as described below.

For each individual M star, we computed a reddening value from each of the three r - i vs. i -J, i -H and i -K diagrams by projecting back the observed colors along the corresponding reddening vector onto one of the possible unreddened theoretical loci⁶. For the objects located bluewards of the related model isochrone, we computed the A_V only if the color is bluer than the related model isochrone by less than the maximum photometric error, e.i. 0.1414 mag. In these cases the A_V is negative but compatible with $A_V=0$.

As discussed before, in the r - i vs. i -J diagram, the theoretical loci of giants, MS and PMS stars almost overlap, and therefore the derived absorption values A_V will be almost independent of the gravity. On the contrary, in the r - i vs. i -H or i -K diagrams, the derived A_V will depend on the gravity, since in these diagrams the loci are quite separated. Therefore, for each star we derive the A_V sets $(A_V^J, A_V^H, A_V^K)_l$ from the three diagrams and each adopted evolutionary status l (with $l=MS$ or G , indicating the loci of MS stars and giants, respectively, or PMS indicating any isochrone with age $\lesssim 10$ Myr). For each given evolutionary status, we derived the means $\langle A_V \rangle_l$, i.e. $\langle A_V \rangle_{MS}$, $\langle A_V \rangle_{PMS}$, $\langle A_V \rangle_G$ and the standard deviations $\sigma(A_V)_l$, i.e. $\sigma(A_V)_{MS}$, $\sigma(A_V)_{PMS}$, $\sigma(A_V)_G$ from the three diagrams. For the case of the PMS state, the A_V calculation includes the multiple Age-Dependent sets of

⁶ The reddening value is converted in absorption by following the relations given in Table 1

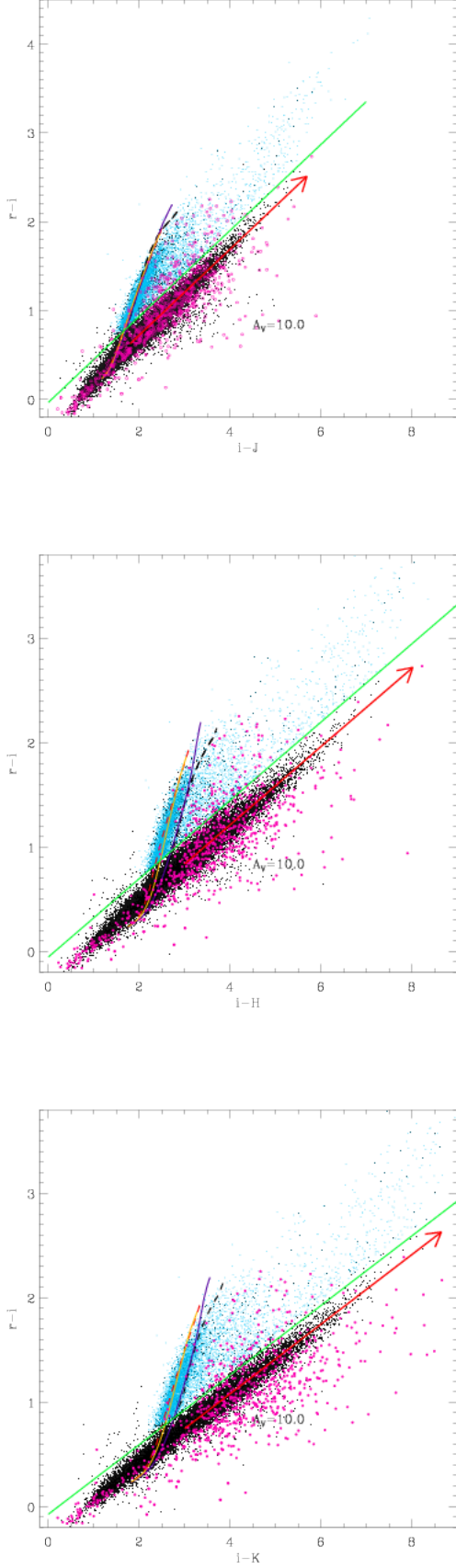


Fig. 13. $r-i$ vs. $i-J$, $i-H$ and $i-K$ diagrams plotted as a two-dimensional stellar density histogram in a grey scale, compared with the MS locus (dashed red line), the 10 Myr and 0.5 Myr isochrones (orange and purple lines) and the giant locus (black line) predicted by PISA models. YSOs selected with *classical* methods and objects selected as M-type stars are indicated with magenta and cyan symbols, respectively. The reddening vectors and the limits used for the selection of M-type stars are indicated as red arrows and green lines, respectively.

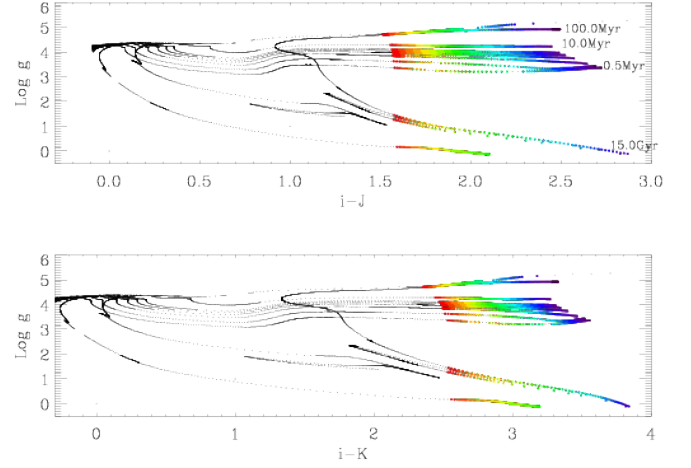


Fig. 14. Log g values vs. $i-J$ (upper panel) and $i-K$ colors (bottom panel), respectively, for a set of solar-metallicity PISA isochrones with ages from 0.5 Myr to 15 Gyr. Different colors indicate different effective temperature values of M-type stars from 3000 K (violet lines) up to 4000 K (red lines) with a step of 50 k.

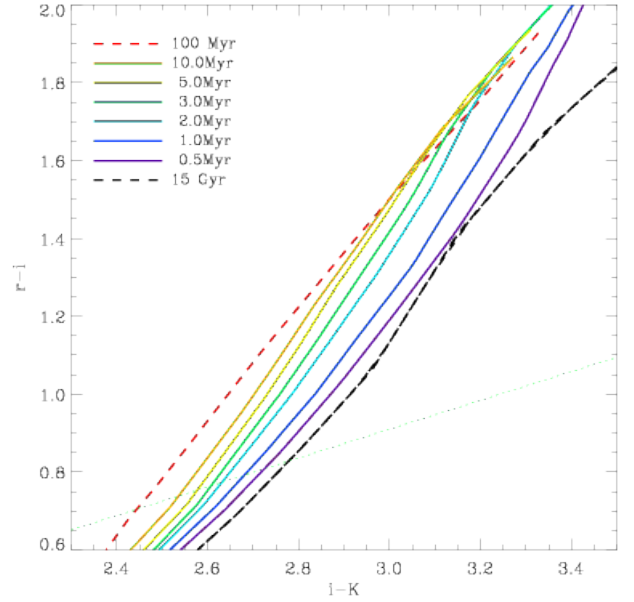


Fig. 15. Zoom of the $r-i$ vs. $i-K$ diagram showing isochrones of different ages. The dotted green line is the limit used to select M-type stars.

(A_V^J , A_V^H , A_V^K) corresponding to the isochrones of 0.5, 1.0, 2.0, 3.0, 5.0 and 10.0 Myr ages.

Clearly, the σ will be large if the adopted evolutionary stage is not the correct one. Thus, we define the best A_V estimate of each star as the mean $\langle A_V \rangle_l$ corresponding to the minimum $\sigma(A_V)_l$.

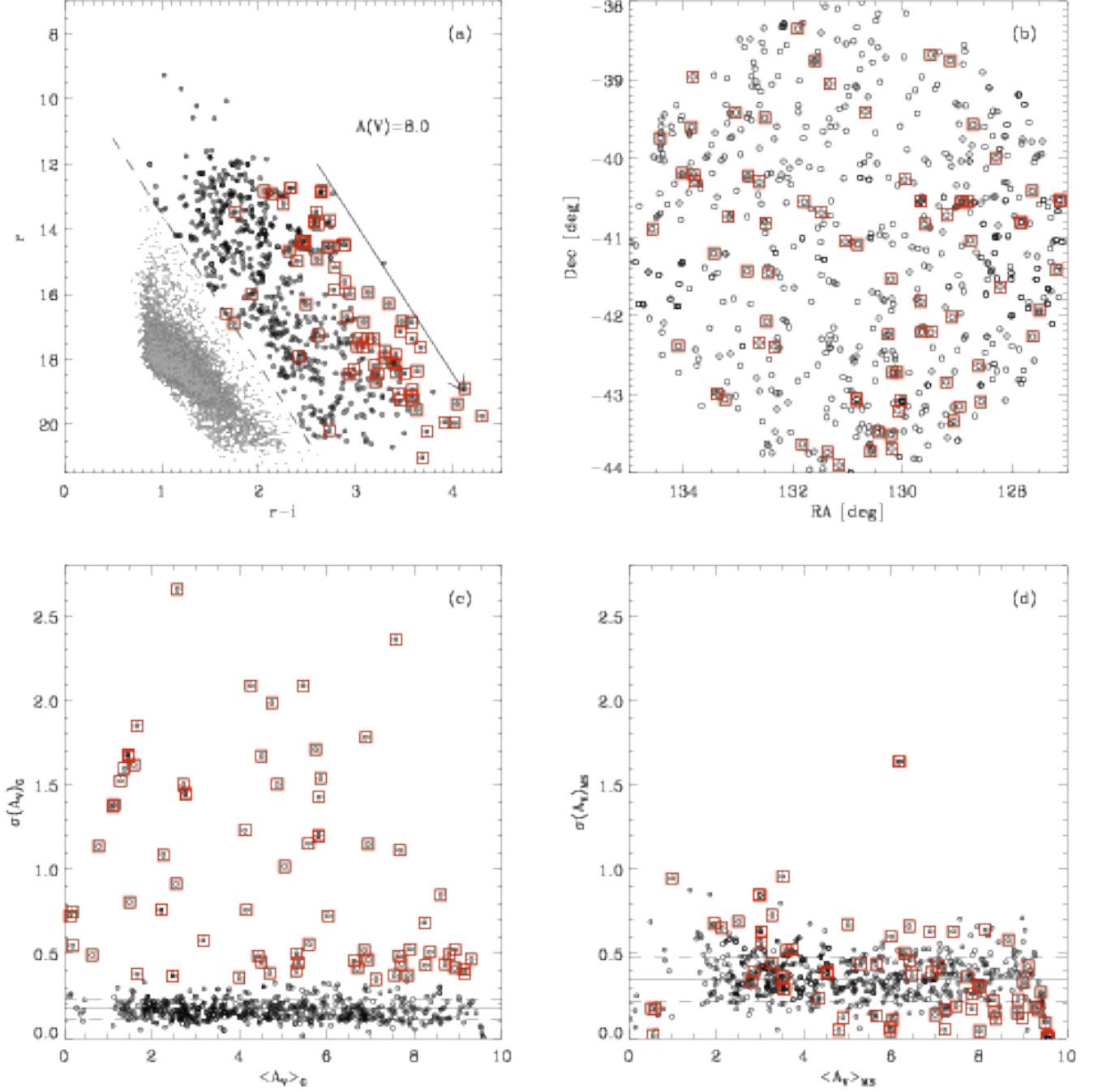


Fig. 16. (a) r vs. $r-i$ diagram of all the objects selected as M-type stars (grey symbols). Black dots are those with r magnitude brighter than the limit indicated by the dashed line, while red squares indicate the subsample including M-type for which the A_V values are not consistent with solar metallicity giants. The reddening vector is also indicated. Spatial distribution (b) and $\sigma(A_V)_I$ vs. the $\langle A_V \rangle_I$ values of bright M-stars, obtained assuming the giant locus (c) and the MS locus (d). The median and the median \pm the pseudo-sigma are indicated by the solid and dashed lines, respectively, in the (c) and (d) panels.

7.1. Bright M-type population

Figure 16 (a) shows the r vs. $r-i$ diagram of the M-type stars. We note that they appear to be grouped in two distinct populations, separated by the dashed line shown in the diagram. We first considered the brightest group to which we will refer to as bright M-type (BM) population and, in particular, we looked at the spatial distribution of this sample, that, as shown in the figure (panel b), does not show any significant clustering. From this distri-

bution, we infer that these objects are not correlated with the young population studied above, but, on the contrary, they are consistent with field M-type MS or giant stars, homogeneously distributed over the region. In order to constrain the luminosity class of these objects, we consider the values of $\sigma(A_V)_{MS}$ and $\sigma(A_V)_G$ defined in the previous section. The results are shown in Figure 16 where we show the scatter plots of dispersion vs. average value for $\langle A_V \rangle_G$ and $\langle A_V \rangle_{MS}$, in panels c and d, respectively.

The $\sigma(A_V)_G$ data show a tail of outliers at high values (red squares). We estimated the statistical parameters of the $\sigma(A_V)_G$ distribution while minimizing the effect of outliers, by computing the median and the pseudo-sigma as the difference between median and the 16th percentile, corresponding to 1σ of a Gaussian distribution $(0.50 - (0.68/2.0)) = 0.16$. The median of the distribution is 0.17 mag while the pseudo-sigma is 0.06 mag. On the contrary, the median of the $\sigma(A_V)_{MS}$ is 0.35 and the pseudo-sigma of 0.13. The first conclusion is that the values obtained assuming the two models show very different shapes. In fact, the $\sigma(A_V)_G$ distribution of most of the objects (black points) shows a very narrow peak, while the $\sigma(A_V)_{MS}$ distribution is much larger. For most of the objects, $\sigma(A_V)_G \ll \sigma(A_V)_{MS}$. This allows us to deduce that for this sample i) the A_V values obtained in each of the CCD by using the giant model are more accurate than those obtained by using the model of MS stars; ii) by computing the mean of the three values associated with the giant model, we obtain not only more accurate but also more precise photometric A_V values; iii) the very narrow peak of the $\sigma(A_V)_G$ distribution of these objects suggests that all of them are consistent with a population of giants rather than MS stars. This latter result is consistent with their position in the r vs. $r-i$ diagram, since it is more likely that very reddened and relatively bright objects like these are M-type giants rather than M-type MS stars.

Finally, we selected 76 objects with $\sigma(A_V)_G > 0.35$ (i.e. larger than 3 pseudo- σ from the median of the distribution) and for which $\sigma(A_V)_{MS} < \sigma(A_V)_G$. For these objects, the quite large spread of the $\sigma(A_V)_{MS}$ values does definitely suggest they are not MS stars. We suspect that the A_V estimates obtained for these objects might not be reliable because we used only solar metallicity models, that are not appropriate if they are M-type stars with non-solar metallicities. As a consequence, with the models adopted in this analysis, we are not able to classify these 76 objects.

In conclusion, from the statistical values, indicated in Figure 16, we deduce that most of the bright M-type stars (551/627) are giants, affected by absorption A_V ranging from ≈ 1.5 to 10, with an error on A_V of about 0.17 (corresponding to the median of the $\sigma(A_V)$ values).

7.2. Faint M-type population

The faint M-type (FM) population includes all objects selected as M-type stars, with r magnitudes fainter than the limit indicated by the dashed line in panel (a) of Fig. 16, shown in the figure with grey symbols.

We expect this population to include field stars as well as YSOs belonging to the clusters we are studying here. Therefore, for each star we computed the triplets $(A_V^J, A_V^H, A_V^K)_{MS}$, $(A_V^J, A_V^H, A_V^K)_G$ and $(A_V^J, A_V^H, A_V^K)_{PMS(t)}$, with t indicating the isochrone ages 0.5, 1.0, 2.0, 3.0, 5.0 and 10.0 Myr.

As done for the BM population, for each triplet, we computed the mean $\langle A_V \rangle_l$ and $\sigma(A_V)_l$ and we considered the best A_V estimate for a given star the $\langle A_V \rangle_l$ for which the $\sigma(A_V)_l$ is smallest.

This condition allows us to derive an A_V more accurate than the one obtained by using only one diagram that could be affected by the possible presence of circumstellar disk, with excesses in one or more of the three J, H or K bands (Cieza et al., 2005). We note that if the M-type stars are affected by strong IR excesses, their colors are redder than the limit adopted to select M-type stars and, therefore, they are not included in the sample of M-type stars. Nevertheless, young M-type stars with small IR

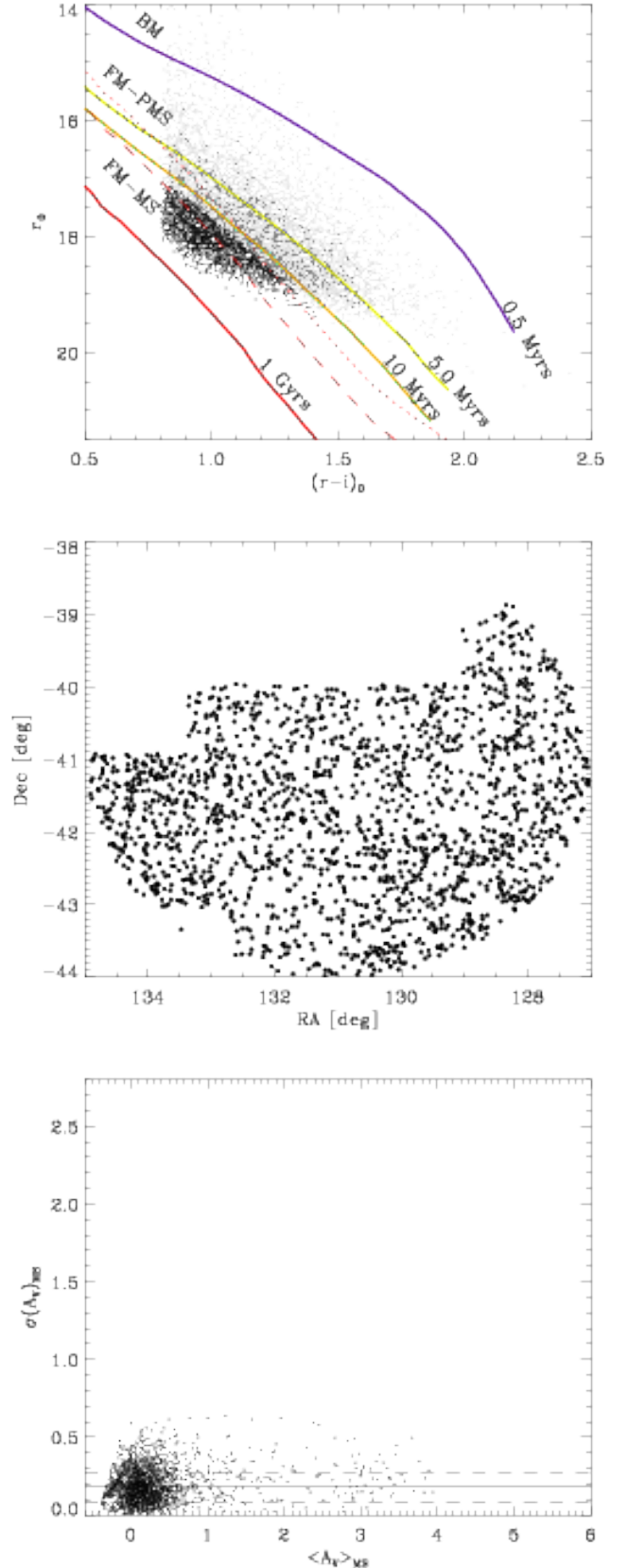


Fig. 17. r_0 vs. $(r-i)_0$ diagram of the faint M-type population (upper panel). Black dots are those selected as MS foreground field stars (see text). Solid lines are the 0.5, 5.0, 10.0 Myr and the 1 Gyr isochrones at the cluster distance. Dotted and dashed lines represent the 1 Gyr isochrone at 300 and 400 pc, respectively. Spatial distribution (middle panel) and $\sigma(A_V)_{MS}$ (bottom panel) of the selected MS foreground field stars. The median and the median \pm pseudo- σ of this distribution are indicated as the solid and dashed lines.

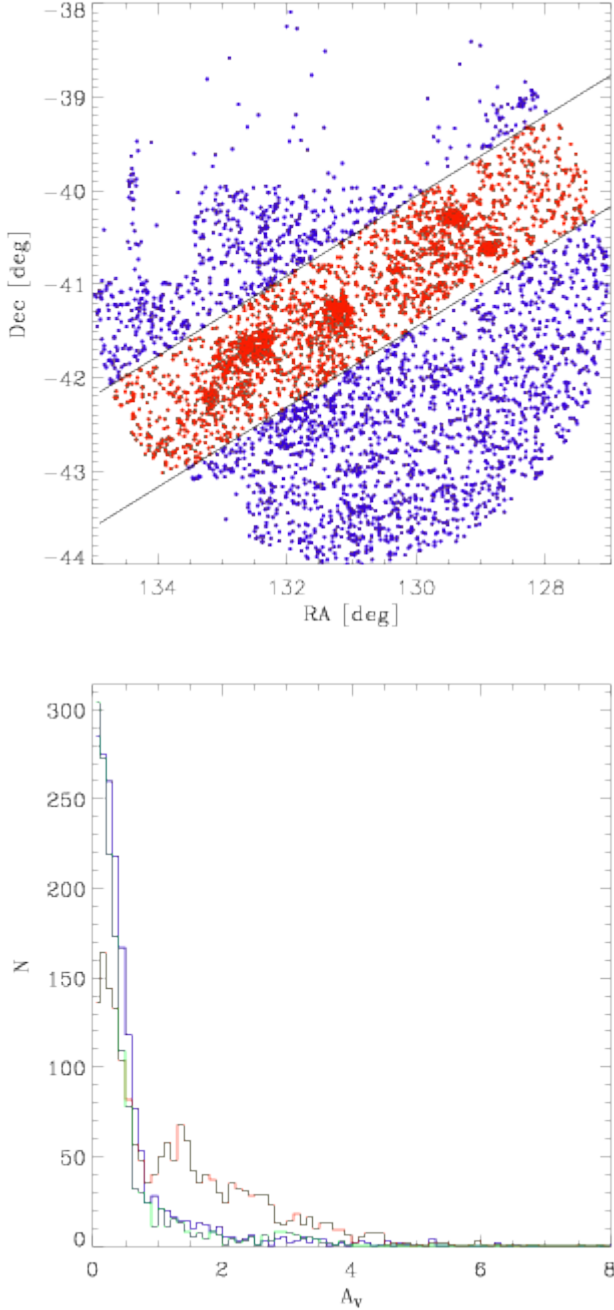


Fig. 18. Upper panel: spatial distribution of the FM-PMS population, divided in two samples, internal (red points) and external (blue point) to the strip arbitrarily defined by the two solid lines. Bottom panel: histograms of the A_V distribution obtained by using the FM-PMS population within the strip (red histogram), FM-PMS population outside the strip (blue histogram) and the MS foreground field stars (green histogram).

excesses can fall in the region of M-type stars. In these cases, the A_V can be affected by the IR excesses and the $\sigma(A_V)$ could be larger than the one derived for disk-less M-type stars. These cases can be considered as candidates M-type young stars with circumstellar disk.

7.2.1. Faint M-type MS stars

As already mentioned, due to the partial overlap of the oldest PMS isochrones with the MS locus and of the youngest ones with the giant locus, PMS stars can be misclassified as MS stars or giants and vice-versa. Therefore, in case of star forming regions, it is not possible to definitively assign the age to the objects. Nevertheless, the best A_V values obtained with this method, within the uncertainties due to the photometric errors and the model accuracy, can be considered reliable to obtain intrinsic colors and magnitudes, since they do not depend on the knowledge of the stellar evolutionary stage but only on the photometric indices.

Fig. 17 shows the unreddened r_0 vs. $(r-i)_0$ diagram, derived from the best A_V values, for the faint M-type population, compared with the 0.5, 5.0, 10.0 Myr and the 1 Gyr isochrones at the cluster distance. In this diagram, the only unknown parameter is the distance but, if we assume that the young population can be found only between the 0.5 and 10 Myr isochrone at the distance of 750 pc (see Sect. 5), we can conclude that all the objects with r_0 larger than the 10.0 Myr isochrone at the cluster distance (to which we added a delta r equal to 0.2 to take into account the errors) are not compatible with YSOs belonging to our clusters and therefore are expected to be field stars. Based on the position of the 1 Gyr isochrone, at the cluster distance, we deduce they cannot be background M-type MS stars but, instead, they are compatible with foreground M-type MS stars with distance smaller than the cluster distance and approximately larger than about 300-400 pc. In fact, the 1 Gyr MS isochrone at 300 pc (400 pc) approximately corresponds to the M-late (M-early) lower limit in r_0 that we adopted to delimit this sample of field stars. Our conclusion is confirmed by their spatial distribution, that is quite uniform, as expected for field foreground stars.⁷ We will refer to this population as the faint M-type MS (FM-MS) stars.

Fig. 17 shows also the $\sigma(A_V)_{MS}$ values as a function of the $\langle A_V \rangle_{MS}$. As done for the giants of the bright M-type population, we computed the median and pseudo- σ of the $\sigma(A_V)_{MS}$ values that are found to be, respectively, 0.18, equal to that of bright giants, and 0.1, larger than the analogous value found for giants (0.06). The larger dispersion derived for MS stars may be due to the very small values of A_V ($\lesssim 0.8$) found for most of these stars. In conclusion, we selected 1869 faint M-type objects that we classify as MS foreground field stars with distances between 300-400 and ~ 750 pc.

7.2.2. Faint M-type PMS stars

In the following, we will analyse the faint M-type population in the PMS photometric region (FM-PMS), i.e. that included between the 0.5 and 10 Myr isochrones at the cluster distance. As already mentioned, this FM-PMS population is expected to include the M-type members of the clusters but also a fraction of contaminating field stars at distance smaller than about 300-400 pc. The spatial distribution of this sample, shown in Fig. 18, shows several clumps of stars, with a pattern very similar to the one found for the YSOs selected with *classical* methods (see Fig. 9), and this suggests that the genuine M-type YSOs are mainly distributed within the spatial strip drawn in the upper panel of Fig. 18 with red symbols. On the contrary, the spatial distribution of the objects outside the strip is quite homogeneous. Therefore, as first approximation, we assume that the FM-PMS

⁷ M-type MS stars at distance smaller than 300-400 pc are, on the contrary, expected to be brighter and therefore overlapping with the PMS region at the cluster distance.

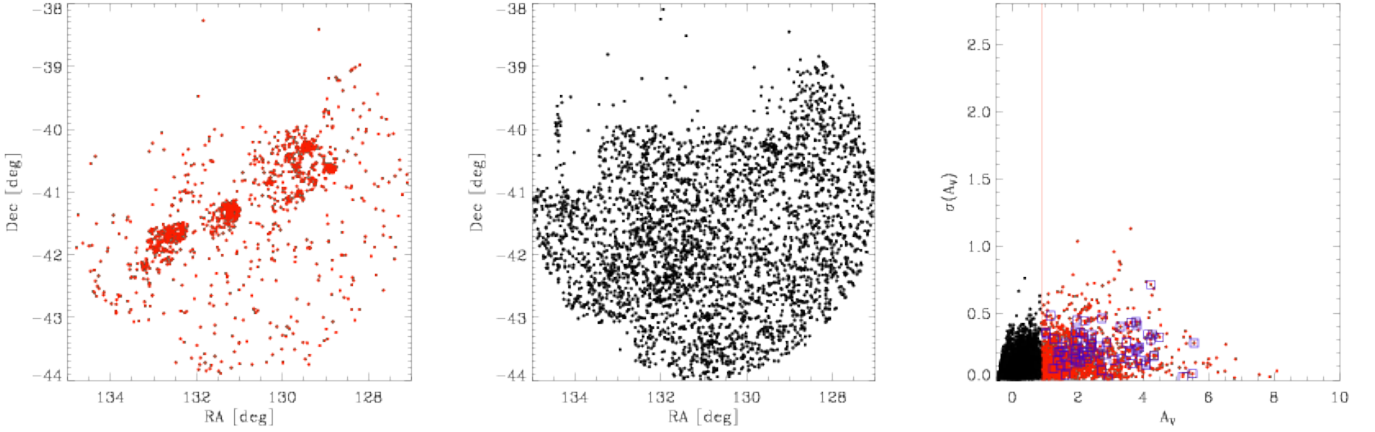


Fig. 19. Spatial distributions (left and middle panels) and $\sigma(A_V)$ vs. A_V (right panel) associated with each star belonging to the red-FM-PMS (red dots) and near-FM-MS (black dots) populations. Blue squares are the objects with disk selected from IR and/or H α excesses.

within the strip is dominated by the young cluster members, while the FM-PMS outside the strip is dominated by the field star population. Figure 18 shows also the histograms of the A_V values for these two populations and for the MS foreground field stars. It is evident that the population dominated by the young cluster members shows two peaks, centered at about $A_V \sim 0.3$ and $A_V \sim 1.5$ while both the other two populations, dominated by the field stars, are very similar and shows a single peak at about $A_V = 0.3$, with a rapid decrease for $A_V \gtrsim 1$. The A_V distribution of the young cluster members shows a minimum at $A_V = 0.9$, corresponding to a sharp drop in the two field distributions. This is the A_V limit that clearly separates the young population from the field population. We cannot exclude that a small fraction of YSOs might be affected by reddening smaller than $A_V = 0.9$ and, vice-versa, a small fraction of MS field stars might be affected by $A_V > 0.9$, like the cluster stars. Nevertheless, the inclusion of this very small fraction of contaminants and the loss of potential few reddened YSOs do not affect our results.

Based on this finding, we split the FM-PMS population in two subsamples, one including objects with $A_V > 0.9$ and the other including the objects with $A_V \leq 0.9$, respectively, to which we will refer as red-FM-PMS and near-FM-MS populations.

Figure 19 shows the spatial distributions of the red-FM-PMS and the near-FM-MS populations. The spatial pattern of the red-FM-PMS population is very similar to that of members selected with other membership criteria (see Fig. 12) and therefore we deduce that the large majority of these objects are genuine members of the three young clusters in RCW 33, RCW 32 and RCW 27. As found by using other methods, there are still candidate members sparsely distributed in the regions outside. Even though they could be less-likely members, we do not attempt to discard them since the shape of the clumps with high density of cluster members is very irregular and we cannot discard the hypothesis that many of them are true YSOs. Therefore, we keep all objects of the red-FM-PMS sample as M-type candidate cluster members. We note that the sample of 907 cluster members, previously selected with classical methods, includes only 84 M-type stars. Among these, 72 (8) belong to the red-FM-PMS (near-FM-MS) populations and are therefore confirmed cluster members. In fact, based on the A_V distribution, we know that a small fraction of cluster members is expected to fall also in the near-FM-MS population, mainly populated by non members. Only 3 ob-

jects belong to the population of foreground stars and one to the BM population.

A very different spatial distribution is, instead, found for the near-FM-MS population. It is quite uniform, even though there is a slightly higher stellar density around RA=131.8 and Dec=-42.4, that corresponds to the nominal centre of the Trumpler 10 association (Kharchenko et al., 2013). The result is better visible if we restrict the analysis to objects within a 0.5 mag strip around a 20 Myr isochrone at the distance of Trumpler 10 (422 pc) found with the PM analysis. However, since the spatial distribution of Trumpler 10 is very sparse, in this work we do not attempt to select its members. Therefore, we classify all the objects belonging to the near-FM-MS population as objects not associated with the three young clusters.

In summary, we have selected 627 objects belonging to the M-type bright population and 6 462 objects of the M-type faint population, for which we derived the individual interstellar reddening. Among the objects in the faint population, there are 1 869 foreground field MS stars with distance larger than 300-400 pc, 3 393 near-FM-MS stars, within the PMS photometric region, affected by small reddening that are not correlated to the young clusters and finally 1 200 FM-PMS stars, that we consider as M-type candidate members of the young clusters.

Figure 19 shows also the $\sigma(A_V)$ as a function of A_V for the red-FM-PMS and the near-FM-MS samples. In this figure, we highlighted the YSOs with IR and/or H α excesses, selected also as M-type stars. We find that very few of them show a $\sigma(A_V)$ significantly larger than the other objects, while the remaining show a $\sigma(A_V)$ distribution very similar to that of the other members. This result suggests that, for the M-type members, the effects due to the presence of circumstellar disk on the A_V values derived with this method can be considered negligible.

8. Discussion

8.1. Spatial distribution analysis

The large number of likely M-type PMS stars selected in this work are consistent with results recently discussed in Damiani (2018) and are related to the higher intrinsic brightness of PMS M-type stars, with respect to MS M-type stars. This implies that at a given mass, a 1 Myr old M star can be detected at a distance much larger than a MS M star (Damiani, 2018). This is a very

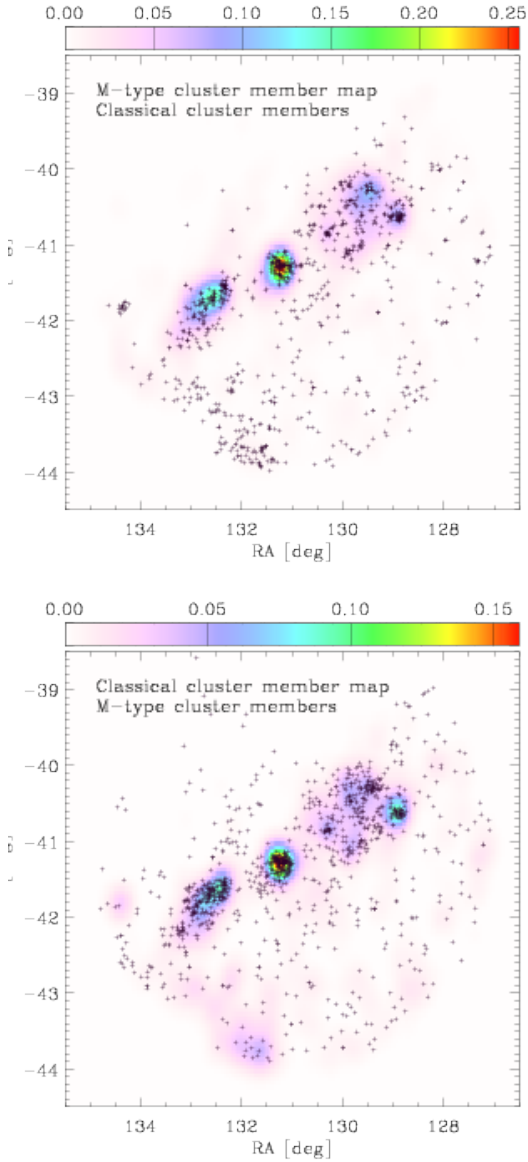


Fig. 20. Upper panel: spatial distribution of cluster members selected as M-type PMS stars in Sect. 7.2.2, plotted as a two-dimensional histogram smoothed with a Gaussian Kernel. The density scale is the number of stars per bin and per arcmin². Overplotted black crosses are candidate members selected with classical methods. Lower panel: spatial distribution of cluster members selected with classical methods, plotted as a smoothed two-dimensional histogram. Overplotted black crosses are cluster members selected as M-type PMS stars.

important property of M-type stars, that has been little exploited up to now in the literature and that, instead, can be used as a very efficient tool to detect the low mass population of YSOs in star forming regions, dominated by M-type stars. In addition, by deriving the individual reddening values using different optical-IR color combinations and the model predictions for different ages, we are able to separate MS and giant M-type stars, mainly expected to be found respectively, at small and large distances from us, and to recognize M-type YSOs.

This result is confirmed from the spatial distributions shown in Fig. 20, for the M-type young cluster members, and for the members selected with classical methods. The coloured maps

are two-dimensional histograms to which we applied a smoothing with a Gaussian kernel.

The comparison of the two spatial distributions shows a clear spatial correlation between the YSOs selected with classical methods and the M-type candidate members selected in Sect. 7.2.2, confirming the peculiar patterns of the three regions, with a more concentrated distribution of YSOs in Cr 197 (RCW 32). The spatial distribution of objects in the cluster Vela T2 (RCW 33) is slightly more sparse with an ellipsoidal shape, while that in Vela T1 (RCW 27) is very sparse with evidence of several clumps.

We verified that the spatial distribution of the faint FM-MS population and that of the objects selected as near-FM-MS and BM (background) giants are not indicative of any significant stellar density clumps, but rather are consistent with a uniform and homogeneous distribution.

8.2. SF history of M-type stars

For the M-type YSOs, we computed stellar ages assuming the distance $d=750$ pc and using the individual reddening values derived in Sect. 7. A minimum and a maximum value to stellar ages have been estimated by considering the photometric errors on r and i and the error on A_V . The A_V and stellar ages of M-type members together with their coordinates and optical/NIR photometry are given in Table 3. Figure 21 shows the intrinsic r_0 vs. $(r-i)_0$ diagrams and the age distributions of the members within the three regions with the highest density, defined in Table 4. Objects have been distinguished in three age ranges, i.e. $t < 2$ Myr, $2 < t/\text{Myr} < 5$ and $t > 5$ Myr. The age distributions of the three clusters show a similar spread with ages from 0.5 to about 13 Myr, but the population of RCW 27 seems to contain a double generation of YSOs, one with median age about 2-3 Myr and another with median age about 5-6 Myr. Figure 22 shows the spatial distributions of the YSOs selected with the classical methods and the M-type YSOs distinguished in the same three age ranges defined above, compared with the dust distribution shown by the IR WISE images at $12\mu\text{m}$, in the three regions with the highest density. The position of the ionizing stars and known clouds in the region are given in Table 5.

For each of the three clusters, Vela T2, Cr 197 and Vela T1, and following the Fasano & Franceschini (1987) approach, we applied the Kolmogorov-Smirnov test on two samples and two dimensions, to the spatial distributions of each pair of subgroups of YSOs with different age. We determined the probability of them being extracted from the same parent distribution, as reported in Table 6, where the p -values are given for each region. We discuss these probabilities in the following sections.

8.2.1. Vela T2 and RCW 33

The WISE image shows two bright clouds, corresponding to the C¹⁸O clouds 14 and 15 of Yamaguchi et al. (1999b) and several bright rimmed clouds (BRC). The two ionizing stars HD75759 and HD75724 lie in the southern region. The first one is a binary with spectral type O9V+B0V, while the second is a B2III star. The first generation of stars ($t > 5$ Myr) are found along the direction defined by clouds 14 and 15, with a higher concentration of stars between the two ionizing stars and cloud 14. The second generation of stars ($2 < t/\text{Myr} < 5$) are mostly found in the same region following the same pattern while the youngest stars ($t < 2$ Myr) mostly formed two clumps around clouds 14 and 15, with few more stars in the middle region, that seems to follow the pat-

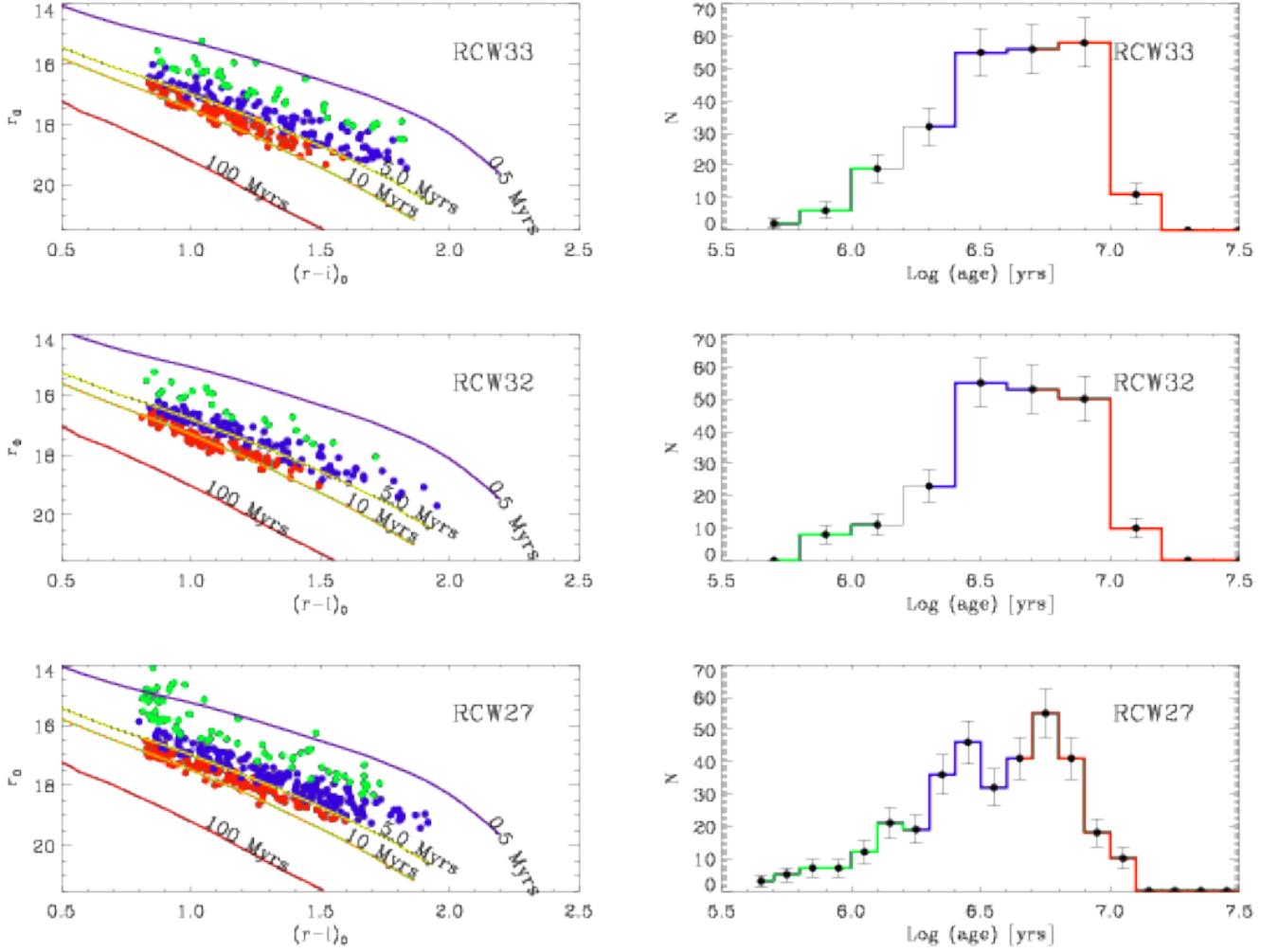


Fig. 21. Intrinsic CMDs and age distributions of the M-type candidate members falling in the three regions defined in Table 4 and grouped in three age ranges, i.e. $t < 2$ My, $2 < t/[Myr] < 5$ and $t > 5$ Myr, indicated with green, blue and red symbols, respectively. Several representative isochrones are overplotted in the CMD.

Table 3. Optical/NIR photometry, A_V and ages of M-type members. Full table available in electronic format only.

CNAME	RA (J2000)	Dec (J2000)	r	i	J	H	K	A_V	Log(t) (yrs)	Log(t) _{min} [yrs]	Log(t) _{max} [yrs]
08475118-3928303	131.96325	-39.47508	14.90	13.87	11.73	10.99	10.72	1.13 ± 0.08	5.00	5.00	5.04
08572585-4026000	134.35771	-40.43334	15.85	14.77	12.59	11.78	11.50	1.28 ± 0.04	5.62	5.52	5.67
08575042-4032562	134.46010	-40.54893	15.06	14.00	11.86	11.06	10.81	1.16 ± 0.02	5.00	5.00	5.00
08472297-3816088	131.84571	-38.26911	15.27	14.07	11.71	10.79	10.49	1.62 ± 0.05	5.00	5.00	5.00
08363711-3824341	129.15461	-38.40948	15.58	14.51	12.41	11.58	11.36	0.91 ± 0.01	5.53	5.50	5.56
08372719-4153363	129.36330	-41.89341	14.55	13.41	11.04	10.27	9.91	1.69 ± 0.12	5.02	5.00	5.15
08372719-4153363	129.36330	-41.89341	14.55	13.41	11.04	10.27	9.91	1.69 ± 0.12	5.02	5.00	5.15
08360090-3941072	129.00376	-39.68533	15.40	14.05	11.28	10.35	9.95	2.74 ± 0.06	5.04	5.00	5.10
08384800-4202113	129.69999	-42.03646	15.69	14.56	12.20	11.59	11.32	1.35 ± 0.36	5.19	5.06	6.27
08310898-3926229	127.78741	-39.43969	16.06	14.82	12.35	11.49	11.17	1.93 ± 0.02	5.03	5.00	5.11

tern defined by the dust density enhancements. The difference between the spatial distributions of the subgroups is not significant or marginally significant with p -values comprising between 0.04 and 0.5.

8.2.2. RCW 32 and Cr 197

In the region of RCW 32, cluster members are found between the SFO 58 and SFO 57 BRCs (Sugitani & Ogura, 1994), associated with the B0 V-B4 II ionizing star HD 74804 (Urquhart et al., 2009). Both SFO57 and SFO58 are included in the sample of candidates for triggered SF (Urquhart et al., 2009), associated to the formation of a photon-dominated region. Our results

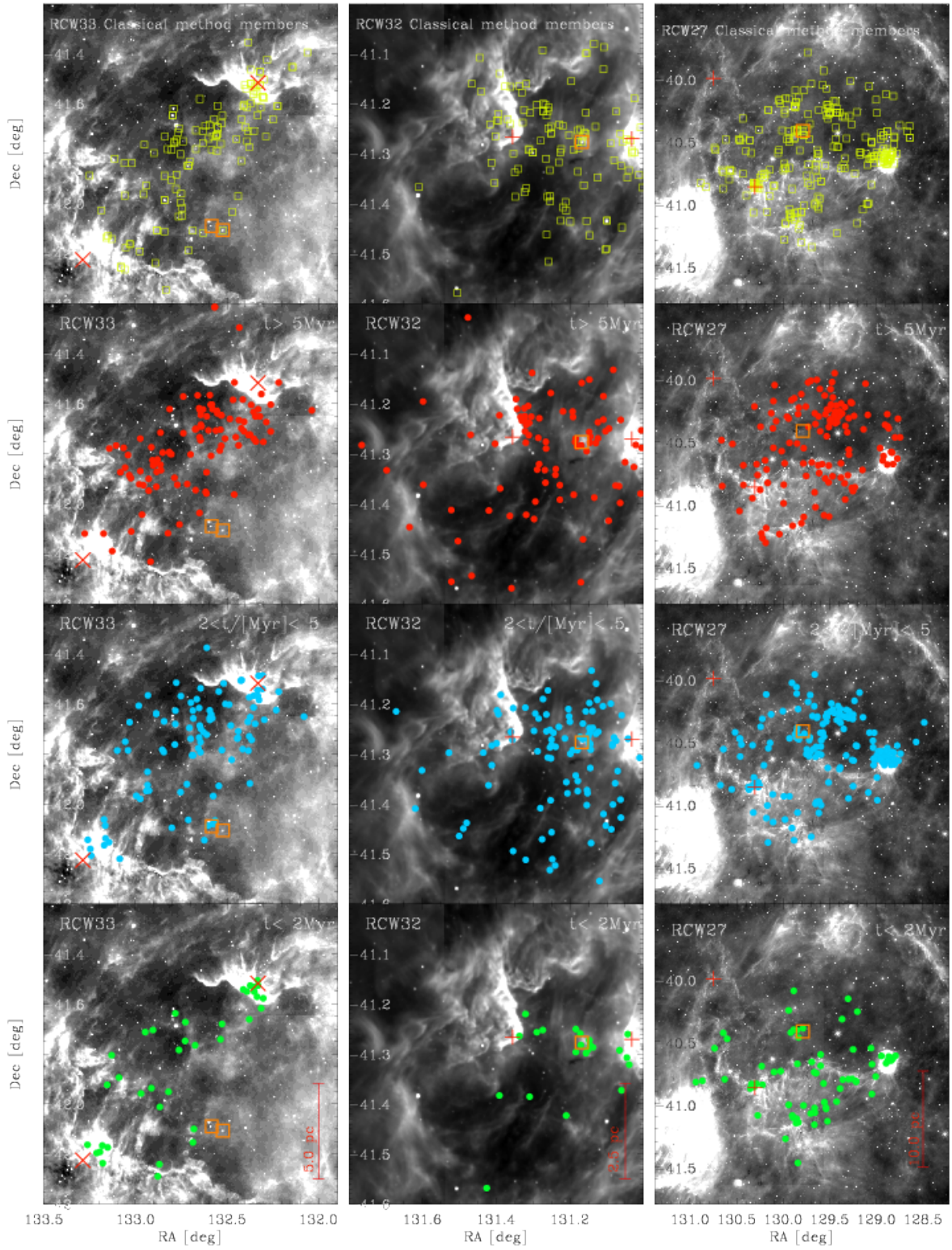


Fig. 22. Different scale WISE images at 12 μm in RCW 33, 32 and 27 in left, middle and right panels, respectively. YSOs selected with classical methods (upper panels) and M-type YSOs in different age ranges (lower panels) overplotted with yellow squares and red, blue and green points, respectively. Orange empty squares indicate the position of the ionizing stars, while red crosses and plus symbols correspond to C¹³O clouds 14 and 15 and to SFO sources, respectively.

Table 4. Galactic coordinates of the boxes around the three H II regions with the highest star density

H II	Min. l	Max. l	Min. b	Max. b
RCW33	262.0	263.2	1.2	1.8
RCW32	261.2	261.9	0.6	1.3
RCW27	259.5	261.1	-0.2	1.2

Table 5. Coordinates of the ionizing stars and of known clouds in the region.

H II	ID	RA [deg]	Dec [deg]
RCW33	HD75759	132.58	-42.09
RCW33	HD75724	132.52	-42.11
RCW32	HD74804	131.17	-41.28
RCW27	HD73882	129.79	-40.42
RCW33	Cloud 14	132.33	-41.52
RCW33	Cloud 15	133.29	-42.23
RCW32	SFO58	131.36	-41.27
RCW32	SFO57	131.03	-41.27
RCW27	SFO56	130.75	-40.00
RCW27	SFO55	130.30	-40.87
RCW27	NGC2626	128.88	-40.67

Table 6. p -values resulting from applying a two-sample K-S test to the spatial distributions of each pair of subgroups with different age.

H II	Age range 1 [Myr]	Age range 2 [Myr]	p -values
RCW 33	[0-2]	[2-5]	0.05
RCW 33	[2-5]	[5-13]	0.5
RCW 33	[0-2]	[5-13]	0.04
RCW 32	[0-2]	[2-5]	0.2
RCW 32	[2-5]	[5-13]	0.15
RCW 32	[0-2]	[5-13]	0.06
RCW 27	[0-2]	[2-5]	0.00006
RCW 27	[2-5]	[5-13]	0.04
RCW 27	[0-2]	[5-13]	0.00006

show that the first generation of stars formed a clump around HD 74804 and another group on the western side, along the direction of SFO 58 and attached to it, while the second generation formed in the middle region between the two BRCs. The few stars formed in the last 2 Myr are concentrated around HD 74804 and in the proximity of the two BRCs. However, the difference between the spatial distributions of the subgroups is not significant with p -values comprising between 0.06 and 0.2.

8.2.3. Vela T1 and RCW 27

In the region of RCW 27, the first generation of stars are found in a clump around (RA, Dec)=(129.25,-40.25) deg, and other stars, some of which concentrated along the bow shape pattern formed by the dust, limited by the SFO 55 BRCs and the reflection nebula NGC 2626, and a second small group of stars, with an elongated distribution, around (RA, Dec)=(129.87, -41.17). The second generation of stars formed two other small clumps of stars in proximity of the O8.5IV star HD73882, a prominent clump around the reflection nebula NGC 2626 and a small clump around SFO 55. More recent SF occurred around NGC 2626, around (RA, Dec)=(129.87, -41.17) and again, along the bow-shape pattern formed by the dust around (RA, Dec)=(129.7, -40.65), going up along the filament formed by the dust. In this

region, the difference between the spatial distributions of the first and the second generation of stars is marginally significant (p -value=0.04) but the difference between the spatial distributions of the youngest stars and the other groups is significant with p -value=0.00006 in both cases.

8.2.4. Concluding remarks

The spatial distribution of the M-type members suggests the formation of several clumps correlated to the stellar ages revealing that SF in young clusters occurs in small subclusters, as predicted by models (Clarke et al., 2000).

For the YSOs selected with the classical methods we are not able to derive accurate individual reddenings and therefore ages. However, the spatial distribution of these objects is consistent with a population formed as the M-type selected members. The spatial distribution of most YSOs in RCW 33 is consistent with that found for the first generation of M-type stars, while that of YSOs in RCW 32 and RCW 27 is better consistent with the one found for the second generation of M-type stars.

Our results suggest a significant age spread with evidence of a continuous SF process that started about 12-13 Myr ago and lasted until less than 1 Myr ago. The age distribution in the three regions is consistent with a decreasing SF rate only in Vela T2 (RCW 33), while the age distribution of YSOs in Cr 197 (RCW 32) might suggest the presence of a triggering process likely due to the ionizing star HD 74804, that is consistent with the scenario suggested by Urquhart et al. (2009) in which the H II region radiation causes the compression and the fragmentation of the material in the molecular cloud.

A strong evidence of triggered SF has also been found in Vela T1 (RCW 27), where several clumps formed with time. The presence of the two peaks in the age distribution suggests a SF acceleration likely caused by the physical interaction between the radiation of massive stars and the surrounding molecular cloud.

To estimate the total number of stars and the total mass of the three populations, we assume a universal Initial Mass Function (IMF) and consider the completeness limits of the magnitudes for M-type stars. that are $r=19.97$, $i=19.09$, $J=15.87$, $H=15.09$ and $K=14.4250$. These values have been estimated at the peak of the magnitude distribution. As described in Damiani (2018), the minimum mass detected at a given distance strongly depends on the age and the absorption A_V (see Fig. 5 of Damiani, 2018). To estimate the lowest mass above which our sample is complete, we used two isochrones at two representative ages for the three regions, i.e. 4 and 5 Myr, and the median A_V of the three regions that are $A_V^{\text{med}}=[1.4,2.5,1.8]$ respectively for RCW 33, RCW 32 and RCW 27. Under these conditions, we estimated that the mass ranges in which M-type stars younger than 4 and 5 Myr and with $A_V < A_V^{\text{med}}$ are all detected are $[0.22-0.94] M_{\odot}$, $[0.34-0.94] M_{\odot}$, $[0.27-0.94] M_{\odot}$ for 4 Myr and $[0.24-0.94] M_{\odot}$, $[0.36-0.94] M_{\odot}$, $[0.28-0.94] M_{\odot}$ for 5 Myr, respectively, for RCW 33, RCW 32 and RCW 27. The upper bound of the mass ranges were derived from the 4 and 5 Myr isochrones for $i-K > 2.2$, that is the color limit used for the selection of M-type stars (see Fig. 13).

In these ranges, oldest and more reddened objects cannot be detected. For each of the three clusters, we counted the number of stars within these mass ranges, with A_V smaller than the median value of each region and ages smaller than 4 (5 Myr) that are 30, 18 and 62 (42, 24 and 64), respectively in RCW 33, RCW 32 and RCW 27. To account for the objects in the same mass ranges, but with ages older than 4 and 5 Myr, we used the fraction of M-type stars in these mass ranges and within the same limits on A_V

but with ages older than 4 (5 Myr), that are 0.70, 0.69 and 0.53 (0.58, 0.55 and 0.47). Finally, we extrapolated the total number of stars of the three populations across the entire mass spectrum by considering the fraction of stars predicted by the Weidner et al. (2010) IMF in the same mass ranges that are 0.34, 0.21 and 0.28 (0.32, 0.20 and 0.27). We thus estimate that the total number of YSOs for the three populations are in the range [124-224], [122-216] and [403-493] stars, respectively, in RCW 33, RCW 32 and RCW 27. If we consider the total mass of M-type stars within the previous mass ranges and consider the mass fraction predicted in the same ranges with the Weidner et al. (2010) IMF, we estimate that the total mass of the three populations is [50-86] M_{\odot} , [45-81] M_{\odot} and [141-174] M_{\odot} . The large uncertainties on these estimates are mainly due to the limited depth of the 2MASS photometry, that hopefully will be overcome by future deep IR surveys covering this region. We note that by using the limit of 4 Myr, the mass ranges are slightly larger than by using 5 Myr and this allows us a slightly less uncertain extrapolation of the IMF, but at the same time we include a smaller fraction of objects from our computation and consequently a larger correction for older stars is necessary. Thus, our choice to consider both two 4 and 5 Myr isochrones enable us to obtain an estimate as reliable as possible, that, however should be considered with caution and, it is likely a lower limit since we did not apply a correction for YSOs with $A_V > A_V^{\text{med}}$.

9. Summary and conclusions

We used optical and NIR photometric surveys to study the young stellar population in the three H II regions RCW 33, 32 and 27 where Pettersson & Reipurth (1994) found signatures of recent SF from H α observations. Using the deeper VPHAS+ survey that covers the region studied by Pettersson & Reipurth (1994), we found 329 YSOs with H α emission showing a spatial pattern that confirms the presence of young clusters associated to the three H II regions. This result prompted the search of the associated population of YSOs surrounded by a circumstellar disk, through NIR surveys, such as SPITZER/GLIMPSE and 2MASS. Using the known properties of YSOs with disk, we selected 559 class II and 20 class I YSOs. We exploited the recent Gaia DR1 to study the kinematic population of the three regions and we found 10, 19 and 25 stars sharing similar PMs and parallaxes in Cr 197, Vela T2 and Vela T1, respectively, confirming the presence of the three clusters, and with a placement in the CMD consistent with PMS stars at the distance of about 750 pc. The distance of the three regions derived from the Gaia data is consistent with that derived from the CMD of the low mass population. Additional YSOs were found by using also archive ROSAT and Chandra X-ray observations. At the end, we selected a total of 907 candidate YSOs in the whole region, with different spatial distribution patterns in the three H II regions.

We added, to this sample, a further sample of 1 200 candidate M-type members. These objects were selected by exploiting two important features of M-type stars, that are the significantly higher luminosity in the PMS phase with respect to MS stars of the same spectral type and the sensitivity of their i-J, i-H and i-K colors to stellar gravity that allowed us to derive the individual reddening independently in three different CCDs, and to select the best A_V value for each M-type star. For the whole M-type population, including the field star population, we therefore derived the unreddened CMD where the only unknown is the distance.

The comparison of the unreddened CMD with PMS isochrones, at the distance of the clusters, allowed us to dis-

card the foreground population of M-type MS stars and the background population of M-type giants. In addition, based on the spatial analysis, we found that the populations of YSOs in RCW 33, 32 and 27 are dominated by objects with $A_V > 1$ and this allowed us to discard also the low reddened ($A_V < 1$) population of M-type MS stars contaminating the photometric PMS locus in the CMD of the clusters.

The spatial distribution of the M-type YSOs is strongly correlated to that of the YSOs selected with classical methods. Since we have a subsample of 72 M-type stars selected with both methods, we find a total population of 2 035 YSOs, mainly distributed inside the three H II regions, presenting for the first time, a stellar census of YSOs in NW-VMR, down to the M-type stars. For the M-type YSO subsample, we also derived stellar masses, down to 0.1 M_{\odot} , and stellar ages in the range 0.5-13 Myr.

We performed a detailed spatial analysis of the M-type members in the three H II regions and compared them with WISE images at 12 μm , that highlights the regions with high concentration of dust. By splitting the M-type YSOs in three different ranges of ages, we found indications on the SF rate. In particular, we found that the formation of YSOs in clumps or in elongated features, is connected to the ages and to the presence of BRCs, visible in the WISE image.

The most likely scenario is that, while the SF rate in RCW 33 is decreasing with time, the SF process in RCW 32 and 27 has been likely triggered by the interaction between the H II radiation associated to the ionizing stars and the molecular clouds from which the low mass star population formed. This scenario is consistent with that suggested by Urquhart et al. (2009), based on CO and mid-IR observations of a sample of H II regions, including RCW 32 and RCW 27.

The criteria used in this work to select M-type stars can be exploited in future works in several contexts of stellar astrophysics. In the context of SF, the intrinsic higher luminosity of M-type stars in PMS phase with respect to MS stars is a new observational diagnostics that allows detection of the M-type young populations of relatively distant regions ($\sim 1-2$ kpc) by using recent photometric surveys. The M-type population in these regions has been up to now mainly revealed by deep and high sensitive X-ray or spectroscopic observations, that are significantly more expensive in terms of telescope time demand. In addition, due to the limited FOV, it is very difficult, if not impossible, to study large fields of several square degrees, as, instead, can be easily done with the current photometric surveys.

The Gaia DR2 data will likely allow a more refined selections since, with the kinematic parameters, it will be possible to confirm M-type candidate members. Moreover, other available and future very deep photometric surveys, such as for example PanSTARRS, UKIDSS, WISE, VVV and LSST, will allow us to detect even more distant M-type stars also in even more distant star forming regions.

Finally, the opportunity to derive accurate individual reddening values of M-type stars is a new tool that can be exploited to discard M-type contaminants, both MS or giants, and therefore to select M-type members, based on the known parameters of the clusters we are dealing with. Moreover, this new diagnostic can be exploited to distinguish M-type MS stars from giants in fields where YSOs are not expected to be found.

Acknowledgements. We wish to thank the anonymous referee for his/her interesting comments and suggestions. This work is based on observations made with ESO Telescopes at the La Silla or Paranal Observatories under programme ID(s) 177.D-3023(B), 177.D-3023(C), 177.D-3023(D), 177.D-3023(E). This work has made use of data from the European Space Agency (ESA) mission *Gaia* (<http://www.cosmos.esa.int/gaia>), processed by the *Gaia* Data Processing

and Analysis Consortium (DPAC, <http://www.cosmos.esa.int/web/gaia/dpac/consortium>). Funding for the DPAC has been provided by national institutions, in particular the institutions participating in the *Gaia* Multilateral Agreement. This publication makes use of data products from the Wide-field Infrared Survey Explorer, which is a joint project of the University of California, Los Angeles, and the Jet Propulsion Laboratory/California Institute of Technology, funded by the National Aeronautics and Space Administration.

References

- Benjamin, R. A., Churchwell, E., Babler, B. L., et al. 2003, *PASP*, 115, 953
- Bonatto, C. & Bica, E. 2010, *A&A*, 516, A81
- Cardelli, J. A., Clayton, G. C., & Mathis, J. S. 1989, *ApJ*, 345, 245
- Churchwell, E., Babler, B. L., Meade, M. R., et al. 2009, *PASP*, 121, 213
- Cieza, L. A., Kessler-Silacci, J. E., Jaffe, D. T., Harvey, P. M., & Evans, II, N. J. 2005, *ApJ*, 635, 422
- Clarke, C. J., Bonnell, I. A., & Hillenbrand, L. A. 2000, *Protostars and Planets IV*, 151
- Crampton, D. & Fisher, W. A. 1974, *Publications of the Dominion Astrophysical Observatory Victoria*, 14, 283
- Cutri, R. M., Skrutskie, M. F., van Dyk, S., et al. 2003, 2MASS All Sky Catalog of point sources. (The IRSA 2MASS All-Sky Point Source Catalog, NASA/IPAC Infrared Science Archive. <http://irsa.ipac.caltech.edu/applications/Gator/>)
- Damiani, F. 2018, ArXiv e-prints
- Damiani, F., Pillitteri, I., & Prisinzano, L. 2017, *A&A*, 602, A115
- de Zeeuw, P. T., Hoogerwerf, R., de Bruijne, J. H. J., Brown, A. G. A., & Blaauw, A. 1999, *AJ*, 117, 354
- Dias, W. S., Alessi, B. S., Moitinho, A., & Lépine, J. R. D. 2002, *A&A*, 389, 871
- Drew, J. E., Gonzalez-Solares, E., Greimel, R., et al. 2014, *MNRAS*, 440, 2036
- Fasano, G. & Franceschini, A. 1987, *MNRAS*, 225, 155
- Gaia Collaboration, Brown, A. G. A., Vallenari, A., et al. 2016a, *A&A*, 595, A2
- Gaia Collaboration, Prusti, T., de Bruijne, J. H. J., et al. 2016b, *A&A*, 595, A1
- Gaustad, J. E., McCullough, P. R., Rosing, W., & Van Buren, D. 2001, *PASP*, 113, 1326
- Georgelin, Y. M., Georgelin, Y. P., & Roux, S. 1973, *A&A*, 25, 337
- Gutermuth, R. A., Megeath, S. T., Myers, P. C., et al. 2009, *ApJS*, 184, 18
- Henden, A. A., Templeton, M., Terrell, D., et al. 2016, *VizieR Online Data Catalog*, 2336
- Indebetouw, R., Mathis, J. S., Babler, B. L., et al. 2005, *ApJ*, 619, 931
- Kenyon, S. J. & Hartmann, L. 1995, *ApJS*, 101, 117
- Kharchenko, N. V., Piskunov, A. E., Röser, S., Schilbach, E., & Scholz, R.-D. 2005, *A&A*, 440, 403
- Kharchenko, N. V., Piskunov, A. E., Schilbach, E., Röser, S., & Scholz, R.-D. 2013, *A&A*, 558, A53
- Liseau, R., Lorenzetti, D., Nisini, B., Spinoglio, L., & Moneti, A. 1992, *A&A*, 265, 577
- Lorenzetti, D., Spinoglio, L., & Liseau, R. 1993, *A&A*, 275, 489
- Marigo, P., Girardi, L., Bressan, A., et al. 2017, *ApJ*, 835, 77
- Massi, F., Giannini, T., Lorenzetti, D., et al. 1999, *A&AS*, 136, 471
- Massi, F., Lorenzetti, D., & Giannini, T. 2003, *A&A*, 399, 147
- Massi, F., Testi, L., & Vanzì, L. 2006, *A&A*, 448, 1007
- Meyer, M. R., Calvet, N., & Hillenbrand, L. A. 1997, *AJ*, 114, 288
- Murphy, D. C. & May, J. 1991, *A&A*, 247, 202
- O'Donnell, J. E. 1994, *ApJ*, 422, 158
- Oke, J. B. & Gunn, J. E. 1983, *ApJ*, 266, 713
- Olmi, L., Ade, P. A. R., Anglés-Alcázar, D., et al. 2009, *ApJ*, 707, 1836
- Pettersson, B. 2008, *Young Stars and Dust Clouds in Puppis and Vela*, ed. B. Reipurth, 43
- Pettersson, B. & Reipurth, B. 1994, *A&AS*, 104
- Randich, S., Tognelli, E., Jackson, R., et al. 2017, ArXiv e-prints
- Stetson, P. B. 1987, *PASP*, 99, 191
- Sugitani, K. & Ogura, K. 1994, *ApJS*, 92, 163
- Testi, L., Vanzì, L., & Massi, F. 2001, *The Messenger*, 103, 28
- Tognelli, E., Prada Moroni, P. G., & Degl'Innocenti, S. 2011, *A&A*, 533, A109
- Urquhart, J. S., Morgan, L. K., & Thompson, M. A. 2009, *A&A*, 497, 789
- Wang, S., Liu, J., Qiu, Y., et al. 2016, *ApJS*, 224, 40
- Weidner, C., Kroupa, P., & Bonnell, I. A. D. 2010, *MNRAS*, 401, 275
- Yamaguchi, N., Mizuno, N., Saito, H., et al. 1999a, *PASJ*, 51, 775
- Yamaguchi, R., Saito, H., Mizuno, N., et al. 1999b, *PASJ*, 51, 791
- Zasowski, G., Majewski, S. R., Indebetouw, R., et al. 2009, *ApJ*, 707, 510